Modeling Mediterranean ocean biogeochemistry of the Last Glacial Maximum

Katharina D. Six[1], Uwe Mikolajewicz[1], and Gerhard Schmiedl[2]

[1]Max Planck Institute for Meteorology, Hamburg, Germany
[2]University Hamburg, Hamburg, Germany

Correspondence: Katharina D. Six (katharina.six@mpimet.mpg.de)

Abstract. We present results of simulations with a physical-biogeochemical ocean model of the Mediterranean Sea for the last glacial maximum (LGM) and analyse the difference in physical and biochemical states between the present day and the past. Long-term simulations with an Earth system model based on ice sheet reconstructions provide the necessary atmospheric forcing data, oceanic boundary conditions at the entrance to the Mediterranean Sea, and river discharge to the entire basin. Our regional model accounts for changes in bathymetry due to ice-sheet volume changes, reduction in atmospheric carbon content, and an adjusted aeolian dust and iron deposition. The physical ocean state of the Mediterranean during the LGM shows a reduced baroclinic water exchange at the Strait of Gibraltar, a more sluggish zonal overturning circulation, and the relocation of intermediate and deep water formation areas - all in line with estimates from paleo sediment records or previous modelling efforts. Most striking features of the biogeochemical realm are a reduction of net primary production, an accumulation of nutrients below the euphotic zone, and an increase of organic matter deposition at the sea floor. This seeming contradiction of increased organic matter deposition and decreased net primary production challenges our view of possible changes in surface biological processes during the LGM. We attribute the origin of a reduced net primary production to the interplay of increased stability of the upper water column, changed zonal water transport at intermediate depths, and colder water temperatures, which slow down all biological processes during the LGM. The cold water temperatures also affect the remineralisation rates of organic material which explains the simulated increase of organic matter deposition, in good agreement with sediment proxy records. In addition, we discuss changes of an artificial tracer which captures the surface ocean temperature signal during organic matter production. A shifted seasonality of biological production in the LGM leads to a difference in the recording of the climate signal by this artificial tracer of up to 1 K. This could be of relevance for the interpretation of proxy records like e.g. alkenones. Our study does not only provide the first consistent insights into the biogeochemistry of the glacial Mediterranean Sea, it will also serve as the starting point for long-term simulations over the entire last deglaciation.

1   Introduction

The Earth climate during the Last glacial maximum (LGM) ~~is~~ was characterized by much colder climate conditions and the existence of massive ice sheets on the northern hemisphere which led to a lowering of the sea level of 70-130 m (Lambeck et al., 2014; Peltier et al., 2015; Tarasov et al., 2012) and significant changes in the atmospheric and oceanic circulation (Löfverström and Lora, 2017) including changes in precipitation and temperature patterns (Kageyama et al., 2021; Löfverström, 2020). These global variations also affect the physical and biogeochemical states of the semi-enclosed Mediterranean Sea (MedSea), which is connected to the global ocean at the Strait of Gibraltar. Today's typical anti-estuarine thermohaline zonal overturning circulation (ZOC) with ~~less saline~~ fresher, and nutrient poor water entering at the Strait of Gibraltar and a salty and nutrient-enriched deeper return flow of primarily Levantine intermediate water masses was slowed down during the LGM (Mikolajewicz, 2011; Colin et al., 2021). Modelling studies indicated that the primary causes of the ZOC variation are the reduced through-flow area at the Strait of Gibraltar at low sea-level stands (Mikolajewicz, 2011; Colin et al., 2021) and an increased water column stability hampering the formation of Levantine intermediate water (Rohling, 1991; Mikolajewicz, 2011). ~~Proxy data from foraminifera shells~~ Water mass proxy data recorded in foraminiferal authigenic fraction confirm reduced water exchange during the LGM between the eastern and the western MedSea basins (Duhamel et al., 2020; Cornuault et al., 2018) and point towards a strong salinity increase in the eastern basin (Thunell and Williams, 1989). The globally more arid LGM climate would support higher salinities, but colder conditions also reduce evaporative fluxes. The net water loss of the MedSea for the LGM is approximately only half of that for modern times (Mikolajewicz, 2011). Tendencies of precipitation and river runoff at the LGM are rather uncertain. A multi-model analysis of paleo-simulations with Earth system models (Kageyama et al., 2021) showed a local precipitation increase over the MedSea, which is also supported by the study of Goldsmith et al. (2017) on long-term water isotopic composition over Israel. In contrast, pollen records concordantly suggest expansion of steppe vegetation and thus significant aridification during the LGM (Allen et al., 1999; Kotthoff et al., 2008; Koutsodendris et al., 2023) and sediment core data which capture climate changes in the Nile catchment rather indicate arid conditions and reduced river discharge compared to present (Box et al., 2011; Revel et al., 2014).

While there are a small number of modelling attempts to reconstruct the physical ocean of the MedSea during the LGM (Myers et al., 1998; Rohling and Gieskes, 1989; Mikolajewicz, 2011), there are none at all published for glacial biogeochemical conditions of the MedSea. Thus, our understanding of tendencies in biogeochemical tracers between past and present stems solely from the interpretation of sediment core data. Lateglacial faunal records from benthic foraminifers indicate that organic matter flux to the seafloor during the LGM was significantly higher than today (Kuhnt et al., 2007; Abu-Zied et al., 2008; Schmiedl et al., 2010). Commonly, it is widely assumed that organic matter fluxes to the seafloor in oligotrophic regions without oxygen limitations are highly correlated to surface primary production (Betzer et al., 1984). As an example, for the present day MedSea, the decreasing primary production from the western to the eastern basin and the concurrent resulting decrease in food availability at the seafloor is clearly reflected in the benthic foraminiferal composition (Rijk et al., 2000). Consequentially, an enhanced organic matter flux during the cold period would point to a higher primary production, quantified, for example, for a single sediment core in the western MedSea (Alboran Sea) which shows a 10 % increase in annual primary production (Radi

and de Vernal, 2008). Benthic foraminiferal stable carbon isotope records suggest approximately 20 % higher glacial primary productivity in the Ligurian Sea but no significant changes in the Strait of Sicily (Theodor, 2016).

Increased LGM primary production due to upward mixing of nutrients into the euphotic layer was also postulated by Rohling and coworkers based on theoretical considerations about a shallowing of the pycnocline position in the eastern basin (Rohling and Gieskes, 1989; Rohling, 1991). However, changes in surface nutrient supply during the LGM are still unclear, which impedes also the interpretation of sediment core data.

We present results of a new model framework (medHAMOCC) to investigate the physical and biogeochemical conditions in the MedSea during the LGM. The setup consists of a regional ocean-biogeochemical model for the MedSea which is forced by unique new data sets from an Earth system model (MPIESM) suitable for long-term paleo simulations (Kapsch et al., 2022). The MPIESM provides all necessary atmospheric and lateral oceanic physical boundary conditions and river runoff from the last glacial to present day (26,000 years) for two different ice-sheet reconstructions (see section 2.2). With these consistent data sets we investigate the mean state of the MedSea for two time slices: the LGM and present day. We also consider changes in bathymetry and in nutrient river loads for the LGM. The efficient performance of the regional MedSea model allows for a 1000 years spin-up run followed by a 1000 years simulation for each time slice. This guarantees a very low model drift and also minimises the impact of initial conditions. Following a model evaluation of present-day conditions (section 3), we address the drivers of circulation changes between past and present and analyse in detail their impact on the biogeochemistry (section 4). An additional sensitivity run is performed to gain further insights into the impact of a changed LGM bathymetry (section 2.3). By introducing a diagnostic tracer to track biological production temperatures, we mimic the information captured in paleo-proxy data records. This gives us the opportunity to investigate potential biases that may occur when recording the climate signal in marine sediment cores (~~subsection~~ section 4.4). Future applications and limitations of our model framework will be discussed at the end of this paper (section 5).

2   Methods

2.1   Model setup

We use a regional setup of the primitive equation ocean general circulation model MPIOM (Mikolajewicz, 2011; Jungclaus et al., 2013; Mauritsen et al., 2019) ~~combined~~ coupled with a comprehensive biogeochemical model HAMOCC (Six et al., 1996; Ilyina et al., 2013) in an updated version of the one used by Liu et al. (2021). This setup is called medHAMOCC in the following. MPIOM is formulated on an Arakawa-C grid in the horizontal and on z-levels in the vertical direction using the hydrostatic and Boussinesq approximations. Subgrid-scale parameterizations include lateral mixing on isopycnals (Redi, 1982) and tracer transports by unresolved eddies (Gent et al., 1995). Vertical mixing is realized by a combination of the Richardson number-dependent scheme of Pacanowski and Philander (1981) and direct wind-driven turbulent mixing in the mixed layer ~~(further details are given in Jungclaus et al. (2013) and Mauritsen et al. (2019))~~(further details are given in Jungclaus et al., 2013; Mauritse . The Mediterranean setup of the MPIOM covers the entire Mediterranean Sea and the Black Sea (Fig. 1). Part of the Atlantic is included as a sponge zone for the open western boundary (~~Fig. 1~~see section 2.2). The numerical grid has a mean
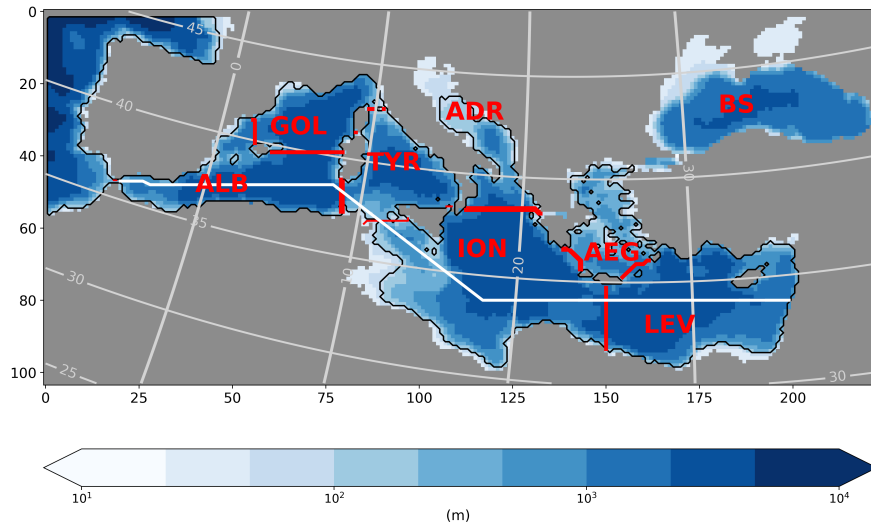
Figure 1. Topography of present day (depth in m) for the entire model domain (225x104 grid cells). LGM shoreline is given by the black contour line. Lightgrey lines give the corresponding longitudes and latitudes. Red lines indicate extension of regions used for basin averages: ALB=Alboran, GOL=Gulf of Lions, TYR=Tyrrhenian Sea, ION=Ionian Sea, LEV=Levantine Sea, AEG=Aegean Sea, ADR=Adriatic, BS=Black Sea. The white line shows the geographical location of the west-east section.

horizontal resolution of approx. 20 km and 42 unevenly distributed layers in the vertical (9 layers in the upper 100 m and increasing ~~layers~~ layer thicknesses to a maximum and constant layer thickness of 150 m below 675 m). The bathymetry for present day and of the Last Glacial Maximum is derived from ice-sheet reconstructions following the method of Meccia and Mikolajewicz (2018). We consider partial grid cells in the last wet grid cell. ~~Fig.~~ Figure 1 shows the present day land-sea mask and basin depth. The overlaid LGM shoreline indicates a closed Bosporus gateway and the desiccation of the northern Adriatic Sea due to low sea level stands (see section 2.3). The same hydrodynamic processes that are resolved for tracers within MPIOM are applied to all tracers of the biogeochemical component HAMOCC (Six et al., 1996; Ilyina et al., 2013; Paulsen et al., 2017). HAMOCC includes a description of the full carbon chemistry, ~~plankton dynamics for phytoplankton, zooplankton~~ the cycling of nutrients (phosphate, nitrate, silicate, iron) and oxygen, and a plankton dynamics with 5 tracers (2 types of phytoplankton, bulk and nitrogen fixers, ~~and~~ one zooplankton type, dissolved and particulate organic matter~~(,~~ the latter called detritus in the following). Phytoplankton growth depends on incoming light at the corresponding depth level, the availability of nutrients and temperature (Paulsen et al., 2017). HAMOCC includes detritus settling and remineralization of dissolved organic matter and detritus (aerobic and anaerobic) ~~, and production, sinking~~ as well as production, gravitational sinking, and dissolution of opal and calcite shells (Ilyina et al., 2013; Mauritsen et al., 2019). ~~Organic matter produced by~~ Shell production is linked to plankton concentration changes with a preference to opal production as long as silicate is available (Ilyina et al., 2013). Organic matter from primary production is composed of carbon, phosphorus, nitrogen, and oxygen according to a constant stoichiometry ~~(C:N:P:O_2=122:16:1:-172, Takahashi et al. (1985))~~ and iron (Fe:P=366

~~10^{-6}, Johnson et al. (1997))~~(C:N:P:O$_2$=122:16:1:-172, Takahashi et al., 1985) and iron (Fe:P=366 10^{-6}, Johnson et al., 1997)
. A sediment module, which consists of solid components (detritus, opal and calcite shells, clay, and sand), includes the same remineralisation and dissolution processes in porewater as in the water column and acts as the lower boundary (Heinze et al., 1999). The sediment module has the same horizontal resolution as medHAMOCC and 12 biologically active levels with in-
110 creasing layer thickness and decreasing porosity from the water-sediment interface to a diagenetically consolidated burial layer.

Two major changes have been introduced in the here applied medHAMOCC compared to the latest version of HAMOCC6 (Mauritsen et al., 2019) :

1) a modified sinking and remineralization process of detritus: in general, gravitational driven detritus fluxes show the shape
115 of a power law function (Martin et al., 1987). Variations in the settling velocity, which are attributed to disaggregation and aggregation of particles or changes in the intensity of remineralisation, e.g. due to temperature dependent bacterial activity, form this curve (Kriest and Oschlies, 2008; Laufkötter et al., 2017). As the exponent of the power law function is given by the ratio of the remineralization rate and the particle settling velocity, a decrease in the remineralisation rate has the same effect on the exponent as an increase in the settling velocity (Kriest and Oschlies, 2008). In HAMOCC6, a depth-dependent detritus
120 sinking speed and a temperature-independent remineralization rate are applied. In view of the large temperature difference between LGM and present day, we introduce a temperature-dependent remineralisation rate (Bidle et al., 2002) and a constant detritus sinking speed in medHAMOCC. The control parameters were optimized to obtain an equivalent result between the two parametrisation approaches for present day. Note, that the remineralisation rate is oxygen-dependent in both HAMOCC versions. 2) a sediment resuspension: we implemented the sediment resuspension scheme developed in Mathis et al. (2019).
125 Depending on grain size, particle density and bottom shear stress, all solid particles (except of sand) from the upper most sediment layer can be remobilized and are relocated or remineralized in the water column.

Additionally, we introduce a tracer (T_{org}) to track the temperature at which primary production takes place. T_{org}, a kind of a phytoplankton twin, is treated by the same biological turnover processes and eventually enters the sediment by organic matter settling. It mimics the information which is implicitly carried by proxy data, such as alkenones. T_{org} gives us the possibility to
130 assess potential biases that may occur when climate signals are recorded by proxy data.

2.2 Forcing and boundary conditions

All necessary atmospheric forcing fields are taken from long-term paleo simulations with an Earth system model ~~(MPIESM, Kapsch et al. (2022))~~(MPIESM, Kapsch et al., 2022). These transient simulations cover the entire period from the last glacial to present day (26,000 years), but we use here only two time slices : the LGM and the preindustrial period (PI). To allow for
135 a consistent spin-up, we take 2000 years transient forcing data for each time slice: LGM (22000-20000 yr BP) and PI (2000-0 yr BP, reference year 1950) and we consider the first 1000 years of each time slice simulation as spinup. Atmospheric forcing data are 2-meter temperature, dew point temperature, downward short and long wave radiation, 10 m wind speed, zonal and meridional wind stress components, and precipitation as monthly averages. The atmospheric model component of MPIESM has a relative coarse horizontal resolution (approx. 3.75°). Therefore, we applied a simple downscaling procedure with bias

140 correction on the basis of reanalysis data ~~(ERA 20C, Poli et al. (2016))~~(ERA 20C, Poli et al., 2016). Heat and freshwater fluxes

over the water are calculated using the standard bulk formulae (Mikolajewicz, 2011; Liu et al., 2021).

A unique feature of these long term simulations with MPIESM is an automatic adaptation of the topography/bathymetry due

to volume changes of ice sheets and isostatic adjustment which is calculated every 10 simulation years (Kapsch et al., 2022).

Corresponding changes of the hydrological discharge and the river routing are also considered (Riddick et al., 2018). For

145 medHAMOCC, we adopt the same automatic adaptation of the topography/bathymetry and consider the transient hydrological

discharge to the MedSea. We add freshwater from the river runoff with a corresponding nutrient load (phosphate, nitrate and

silicate). This nutrient load is deduced from simulated freshwater discharge multiplied with a mean river nutrient concentration

for individual basins of the Mediterranean Sea and the Black Sea to account for temporal variability in nutrient supply. We

derive the basin mean nutrient concentration from modern nutrient input estimates (Ludwig et al., 2009) divided by the simu-

150 lated mean basin river discharge of the last 10 years of the MPIESM simulation. This procedure guarantees a realistic nutrient

supply for present day despite a potential river discharge bias in the parent simulation. Aeolian clay and iron deposition for the

PI and the LGM is taken from Albani et al. (2016).

~~At the open boundaries~~ The western/northern boundary of the model domain ~~towards~~ in the Atlantic Ocean ~~, we include a~~ is a

solid wall with an adjacent sponge zone of about 80 km over which ocean temperatures and salinities are relaxed to correspond-

155 ing monthly mean data from the MPIESM simulation with a relaxation time of 1 month. These boundary conditions of MP-

IESM have been bias-corrected by the difference between the mean of the last 100 yr of the MPIESM simulation and a clima-

tology for temperature and salinity ~~(PHC, Steele et al. (2001)). Sea~~ (PHC, Steele et al., 2001). To guarantee a nearly constant

water volume in the model domain and a consistent water flux at the Strait of Gibraltar, sea level is relaxed to zero in the sponge

zone. All biological organic components (e.g. phytoplankton) are relaxed to their prescribed minimum concentration. For

160 other biogeochemical tracers we use climatological monthly mean data from the World Ocean Atlas ~~(Garcia et al. (2019a, b)~~

~~, phosphate, nitrate, oxygen, and silicate)~~ (phosphate, nitrate, oxygen, and silicate, Garcia et al., 2019a, b) and climatological

annual mean data from GLODAPV2 ~~(Lauvset et al. (2021), dissolved inorganic carbon, and alkalinity)~~(dissolved inorganic carbon, and alk

. We are aware of the inconsistency to prescribe modern concentrations in the sponge zone in a LGM simulation. However,

estimates on nutrient concentrations for the LGM remain a challenge. Tamburini and Föllmi (2009) suggested an overall in-

165 crease of the global phosphate inventory of 17-40 % between LGM and present day. Some sediment records along the Iberian

margins (Kohfeld et al., 2005; Radi and de Vernal, 2008) and a few modelling studies (Bopp et al., 2003; Menviel et al., 2008;

Palastanga et al., 2013) point towards higher ~~primary~~ export production in the ~~North Atlantic~~ eastern side of North Atlantic

between 0-40° N as a result of enhanced nutrient upwelling and/or nutrient supply from shelf areas due to sea level low stands.

However, a higher global phosphate inventory does not imply that surface nutrient concentrations are also higher in the North

170 Atlantic (Bopp et al., 2003; Morée et al., 2021) and that more nutrients would enter the Mediterranean Sea. Therefore, we stick

to present day's values for the prescribed boundary conditions in the sponge zone.

2.3 Set of experiments

From MPIESM, we use forcing data sets from two simulations based on different ice sheet reconstructions (GLAC-1D, Tarasov et al. (2012) and ICE-6G, Peltier et al. (2015), see ~~Tab.~~ Table 1). Differences in these "parent" simulations arise primarily from the temporal change in ice volume and its impact on the atmospheric circulation, as well as the freshwater discharge from ice melt affecting sea surface salinity and, consequentially, ocean meridional overturning circulation in the North Atlantic (Kapsch et al., 2022). Estimates of different ice sheet volumes during the LGM for GLAC-1D and ICE-6G lead to different eustatic sea level changes of about 70 m and 100 m, respectively. Consequentially, the present day sill depth at the Strait of Gibraltar (297 m) shallows to 216 m in GLAC-1D and 200 m in ICE-6G. By applying forcings from different ice sheet reconstructions, we capture uncertainties resulting from glacial boundary conditions. Each parent simulation provides 2000 years of a consistent forcing for the LGM (22000-20000 yrs BP) and preindustrial (2000-0 yrs BP with a reference year of 1950) time slices. Our results are shown as means for the last 1000 years of each simulation with an exception for the model-data comparison with the MEDATLAS (MEDAR Group, 2002) when we use only the last 70 years of the PI simulation of GLAC-1D and ICE-6G.

In addition, we perform a sensitivity study with the present-day GLAC-1D forcing to assess only the impact of shallower sill depths ~~at Gibraltar and in~~ of the Strait of Gibraltar and of the Strait of Sicily on the circulation of the MedSea. To this end, we reduce the sill depth ~~at~~ of the Strait of Gibraltar and the Strait of Sicily to LGM values (216 m for the Strait of Gibraltar and 252 m ~~at~~ for the Strait of Sicily) in experiment PI-Straits (Table 1). The remaining bathymetry is unchanged.

Experiment name	Climate forcing	maximum sill depths (m)	
		Strait of Gibraltar	Strait of Silicy
GLAC-1D	PI with Tarasov et al. (2012)	297	355
	LGM with Tarasov et al. (2012)	216	252
ICE-6G	PI with Peltier et al. (2015)	297	355
	LGM with Peltier et al. (2015)	200	237
PI-Straits	PI with Tarasov et al. (2012)	216	252

Table 1. List of experiments and their major differences.

3 Assessment of the physical and biogeochemical state of the PI

Before we discuss the LGM results, we briefly assess the performance of the physical and biogeochemical state for the PI simulations. Both simulations show very similar results for temperature and salinity for the PI, which is attributable to the very similar PI states of the parent simulations. The basin-wide average of temperature for the Gulf of Lions (GOL, Fig. 2a) agrees quite well with the data compilation of the MEDATLAS (MEDAR Group, 2002), but model results are slightly too cold for the Levantine basin (LEV, Fig. 2e). Both mean salinities of the basins are fresher (0.2-0.6) compared to the observations, but the

	OBS	GLAC-1D		ICE-6G	
		PI	LGM	PI	LGM
precipitation	20.3±3.5 to 47.1±4.4	40.5	39.7	38.5	40.7
evaporation	-90.1±7.1 to -86.8±4.7	-110.2	-84.6	-110.7	-88.5
river runoff	11.2±1.7 (+6.3±3.5)	4.53(+1.6)	5.76	4.35(+1.0)	6.39
net flux	~~-52.~~-52.3±8.7 to -22.2±8.7	~~-65.1~~-63.6	-39.1	~~-67.8~~-66.8	-41.4

Table 2. Hydrological bugdet of the Mediterranean Sea for present day from observations ~~(OBS,Sanchez-Gomez et al. (2011))~~ (OBS, Sanchez-Gomez et al., 2011) and of PI and LGM for GLAC-1D and ICE-6G. Numbers given in 1000 m^3 s^{-1}. For OBS, numbers are converted from mm yr^{-1} with an area for the Mediterranean of 2.5 10^{12} m^2. Numbers in brackets for river runoff gives the Black Sea contribution for PI. The Bosporus gateway is closed during the LGM.

simulated surface salinity difference between GOL and LEV (0.76-0.82) is comparable to the observed one (approx. 1). Note,
195 that we used only the last 70 years of the PI simulations for this model-data comparison.

The MedSea is an evaporative basin where evaporation exceeds precipitation and river input (~~PEM~~ PR-E = ~~preciptation~~ precipitation + river runoff - evaporation). Surface salinities are the result of the interplay between the net water budget, basin water residence time and the salinity signal of inflowing North Atlantic water. Simulated absolute ~~PEM (69-72~~ PR-E (63-67 1000 m^3 s^{-1} in both PI simulations) is slightly higher than observational estimates (22-52 1000 m^3 s^{-1}, Rohling et al.
200 (2015) and refs within; Sanchez-Gomez et al. (2011)) and simulated river runoff to the entire MedSea including the Black Sea contribution at the Bosporus (in total about 5-6 1000 m^3 s^{-1}) is much lower than the observational estimates (Dubois et al. (2011): 17.5 1000 m^3 ~~s^{-1}~~ s^{-1}, Ludwig et al. (2009): 13.6-23.3 1000 m^3 s^{-1}) (Table 2). Our atmospheric parent model, which has a very coarse horizontal resolution (3.75°), potentially underestimates the total runoff to the entire region as already shown for MPI-ESM model versions with even higher spatial resolution (Sanchez-Gomez et al., 2011). The net water loss through
205 evaporation is compensated by a net inflow of Atlantic water (+0.06-0.076 ~~Sv~~ Sv, 1 Sv =10^6 m^3 s^{-1}) which is within the range of observational estimates ~~(+0.04-0.11 Sv, Candela (2001); Tsimplis and Bryden (2000))~~(+0.04-0.11 Sv, Candela, 2001; Tsimplis and Bryde
. Figure 3 shows the individual in- and outflow contributions for PI which are with 1.15-1.25 Sv at the upper end of range of estimates (e.g. for the outflow, Tsimplis and Bryden (2000) : 0.78 Sv, Candela (2001) : 0.97 Sv, Lacombe and Richez (1982) : 1.15 Sv). The simulated net heat budget (-6 to -4 ~~W~~ W m^{-2}) compares well to observational estimates ~~(-7 to -1 W m^{-2},~~
210 ~~Dubois et al. (2011))~~ (-7 to -1 W m^{-2}, Dubois et al., 2011) (Table 3).

The simulated thermohaline circulation shows the characteristic clockwise zonal overturning pattern between 5° W and 25° E in the upper 1000 m with a maximum strength of more than 1 Sv for the PI (Fig. 4) which is in line with data estimates from Pinardi et al. (2019) or other regional modelling studies ~~(Mikolajewicz, 2011; Adloff et al., 2011; Sevault et al., 2014)~~
215 (Mikolajewicz, 2011; Adloff et al., 2011; Sevault et al., 2014; Reale et al., 2022). The second typical feature is a counter clockwise circulation in the deep eastern MedSea between 15 ~~°~~° E and 32° E which indicates deep water formation. These in-
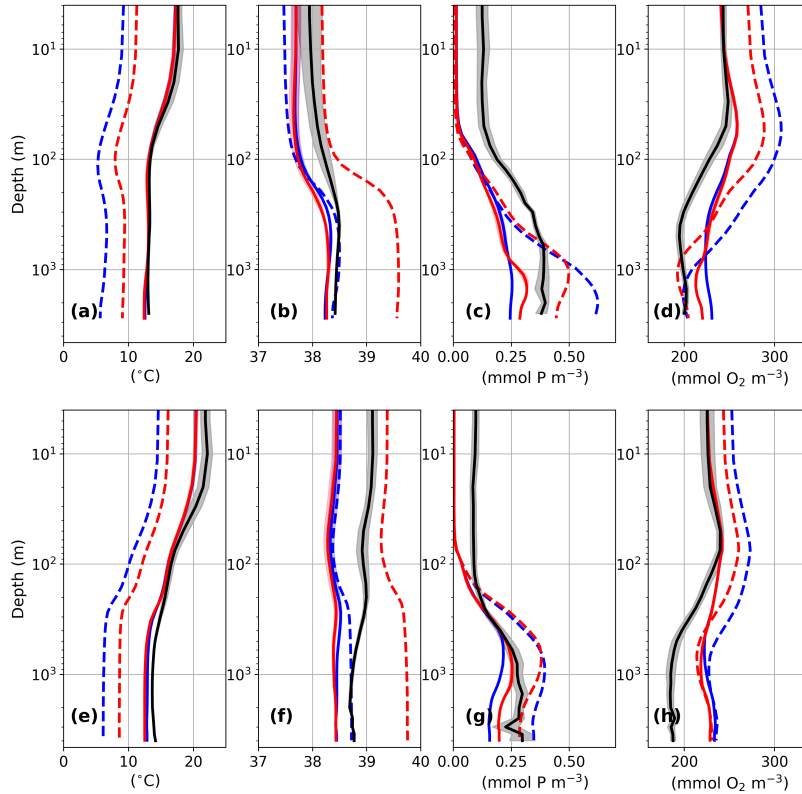
Figure 2. Basin-wide averages for temperature (a, e, °C), salinity (b, f), phosphate (c, g, mmol P/m^3), and oxygen (d, h, mmol O$_2$/m^3) for the Gulf of Lions (GOL, a-d) and the Levantine (LEV, e-h) for GLAC-1D (blue) and ICE-6G (red). Solid lines refer to the PI, dashed lines to the LGM. The black line indicates basin-wide averages of observations (MEDAR Group, 2002) including their standard deviations (grey shading). For this comparison to observations we averaged only over the last 70 years of the PI simulations. Note the logarithmic depth axes. See Fig. 1 for basin definitions.

	OBS	GLAC-1D		ICE-6G	
		PI	LGM	PI	LGM
absorbed shortwave rad.	187±3	198.9	204.1	199.1	206.9
net longwave radiation	-84±1	-75.2	-81.	-75.5	-82.6
latent heat flux	-90±7	-112.3	-97.4	-112.7	-104.5
sensible heat flux	-14±2	-16.4	-31.8	-16.5	-24.7
total	-1±8	-5.0	-6.0	-5.6	-4.8

Table 3. Annual mean heat fluxes of the Mediterranean Sea (W m^{-2}) from observations (OBS, Sanchez-Gomez et al. (2011)) and of PI and LGM for GLAC-1D and ICE-6G
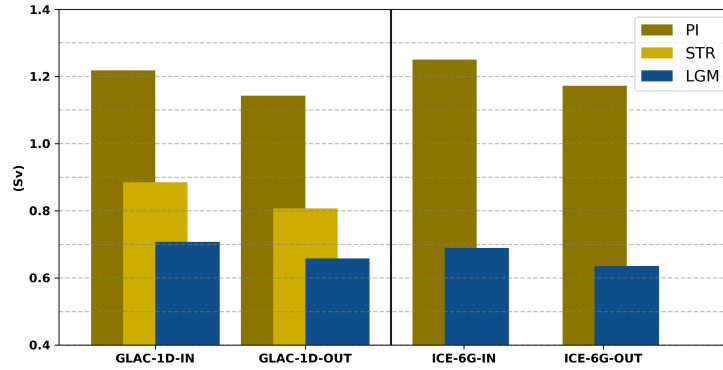
Figure 3. Baroclinic water transport (Sv) at the Strait of Gibraltar separated into in- and outflow components for the PI (brown bars) and the LGM (blue bars) of GLAC-1D and ICE-6G. Golden bars indicate the results of PI-Straits (STR). See also legend in the upper right corner.
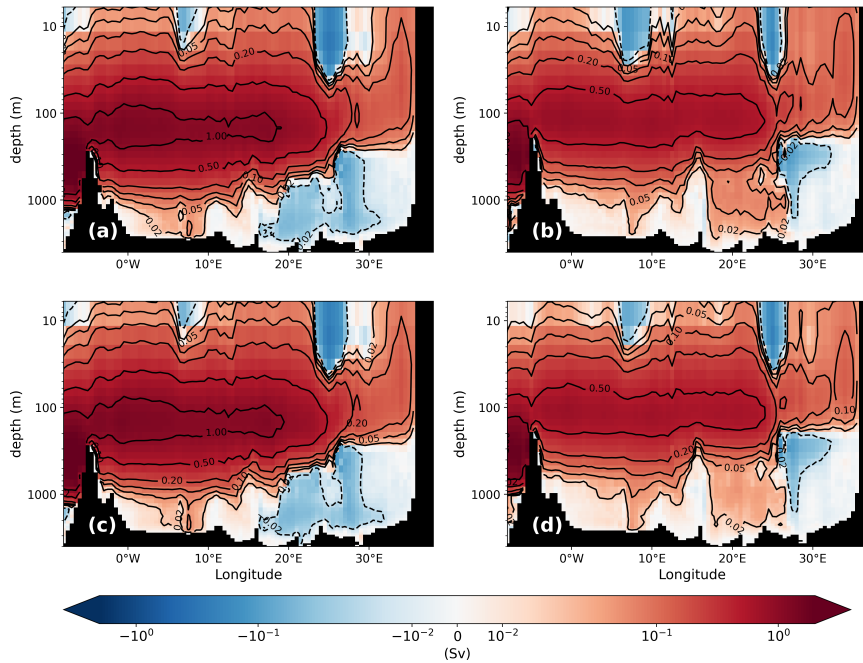
Figure 4. Mean zonal stream function (Sv) of GLAC-1D (a, b) and ICE-6G (c, d) for the PI (a, c) and the LGM (b,d). Contour lines are given as dashed line for (-0.02), and as solid lines for (0.02), (0.05), (0.1), (0.2), (0.5), and (1.0). Please note the logarithmic depth scale and the logarithmic color scale.

termediate and deep water formation areas in the PI are located in the Gulf of Lions, the southern Adriatic Sea, and the southern Aegean Sea which is indicated by the maximum annual mixed layer depth (Fig. A2). The maximum strength of this deep counter clockwise cell in the PI (0.08-0.095 Sv) is slightly weaker than estimates from other modeling studies (Mikolajewicz, 2011; Adloff et al., 2011; Sevault et al., 2014)(0.1-0.3 Sv Mikolajewicz, 2011; Adloff et al., 2011; Sevault et al., 2014; Re, which is a consequence of the reduced variability of the applied monthly mean forcing and the long averaging period (here over 1000 years).

All simulated biogeochemical patterns of the PI reflect the typical west-east gradient. Higher nutrient surface concentrations and a correspondingly higher net primary production (NPP) are found in the western basin, while more oligotrophic conditions are simulated for the eastern basin, with the exception of the region downstream of the Nile river mouth (Fig. 5a). Note, that our simulation is based on conditions prior Nile damming. the construction of the Aswan High Dam in 1964. High NPP is found in the Alboran Sea and in the modified Atlantic water flowing along the coast of Africa into the Ionian Sea. A local high is also found in the GOL, fueled by nutrient supply due to deep winter mixed layers. The oligotrophic eastern Levantine has the lowest net primary production, about half that of the GOL, which is in line with observational estimates (e.g. Uitz et al. (2012)). Compared to satellite derived estimates from Uitz et al. (2012), our simulated NPP is rather on the low side, but fits well within the range of other modelling studies (Table A1). However, the absolute value of the NPP is not so relevant for our study. The amount of exported nutrient from the surface layers below the euphotic zone is more important, as it shapes the nutrient profile.

Basin-wide mean phosphate profiles below 100 m fit well to observations (Fig. 2c, g) with sightly lower concentrations below 1000 m. Simulated mean surface concentrations in the euphotic zone (upper 100 m) are rather low compared to ME-DATLAS in all basins. However, revisiting the climatological mean concentrations of the upper 150 m for 1981-2017 by Belgacem et al. (2021) showed that the climatology of the MEDATLAS has the tendency to overestimate the nutrient concentration, e.g. in the Gulf of Lions. Oxygen concentration below the euphotic zone are slightly higher than the climatology (20-40mmol mmol O_2/m^3). Part of this discrepancy could be related to the missing anthropogenic nutrient input (riverrine and atmospheric) which increased dramatically after 1950 for N and P (Krom et al., 2014). Other nutrient sources like the simulated N-fixation show also higher values in the western basin than in the eastern basin, which is in line with observations (Krom et al., 2014), but they play overall a negligible role (not shown).

Biogeochemical settling processes do not only shape the vertical profiles, but also leave their imprint in the sediment. The spatial pattern of the sedimentation rate of organic material reflects primarily the local ocean depth (Fig. 5b). In the deep basins of the eastern MedSea, the sedimentation flux is less than 1 mgC m^{-2} yr^{-1} compared to a vertical integrated net primary production of approximately 40 gC m^{-2} yr^{-1}. Only the shallower shelf areas receive higher organic matter fluxes as well as a higher deposition fluxes of opal shells, which is clearly visible in the weight-percentage contributions of detritus and opalin the upper 6 mm of the sediment column (first two layers) (Fig. 6). Note, that the remaining percentage part consists primarily of calcium carbonate (CaCO$_3$) and terrigenous material (Fig. A3). The largest weight-percentage contribution of 40-70 % provides CaCO$_3$, where the pattern is very similar to the pattern of NPP. Similar carbonate contents have been documented in sediment cores from different Mediterranean basins (Aksu et al., 1995; Hoogakker et al., 2004; Hamann et al. ,
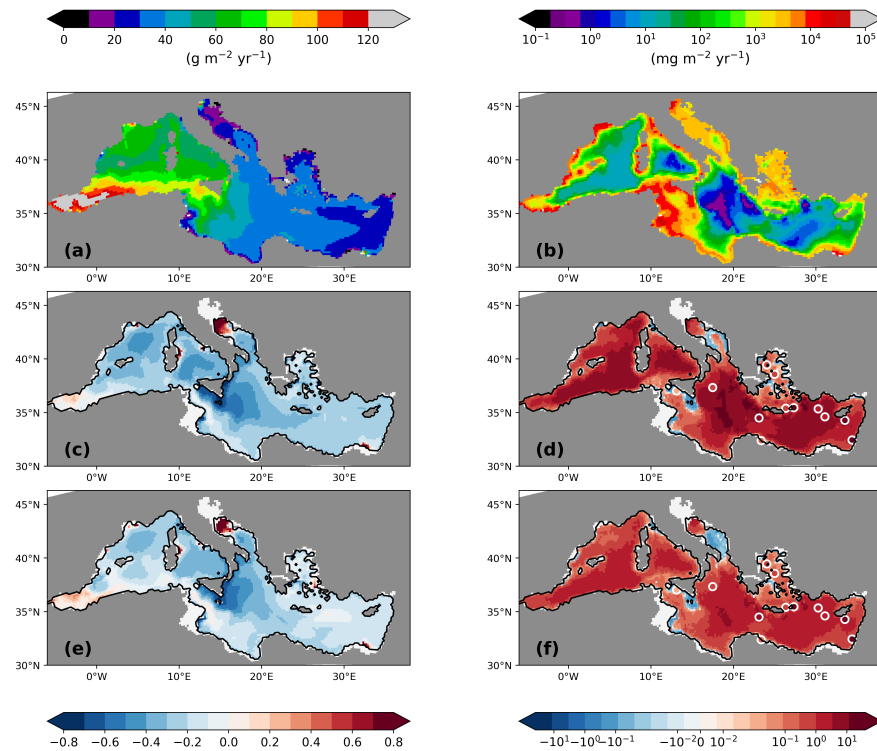
Figure 5. Vertical integrated net primary production NPP (a, gC m^{-2} yr^{-1}) and settling flux of organic material into the sediment (b, mgC m^{-2} yr^{-1}) for the PI of GLAC-1D and the relative changes between the LGM and the corresponding PI for NPP of GLAC-1D (c) and ICE-6G (e) and for the sedimentation rates of GLAC-1D (d) and ICE-6G (f). Note the logarithmic color scales in (b), (d), and (f). The black contour line indicates the LGM coastline. Overlaid circles in (d) and (f) are relative changes in benthic forminiferal numbers between LGM and PI (Schmiedl et al., 2010, 2023).

~~2008)~~(Aksu et al., 1995; Hoogakker et al., 2004; Hamann et al., 2008). The simulated CaCO$_3$ pattern with lower values in the north-east Levantine and higher values in the Ionian Sea towards the Strait of Sicily agrees qualitatively well with the data compilation of Venkatarathnam and Ryan (1971). Supersaturation of the entire water column in the MedSea with respect to calcite prevents dissolution of CaCO$_3$ shells (Béjard et al., 2023) and maps the pattern of planktic calcite shell production on the seabed. For detritus and opal shells, remineralization and dissolution reshape the particle settling fluxes, which decrease with increasing water depth. The sediment in all deep basins consists to less than 0.01 % of detritus or opal shells. Only in the shallower shelf areas 1-2 % weight-percent of the sediment are detritus and 2-10 % are opal shells. Given the simplicity of the sediment module and the coarse horizontal resolution of the medHAMOCC, these results fit very well of the few available core top data for present day (Pedrosa-Pàmies et al., 2015). Sediment erosion, i.e. resuspension of all solid sediment material with the exception of sand, occurs primarily in the ~~Straits~~ Strait of Gibraltar, the ~~Straits~~ Strait of Sicily, and near shore on the Tunisian shelf. However, the simulated resuspension is probably underestimated due to the reduced variability of monthly mean forcing data, but observational data are missing to evaluate our model results.

255

260
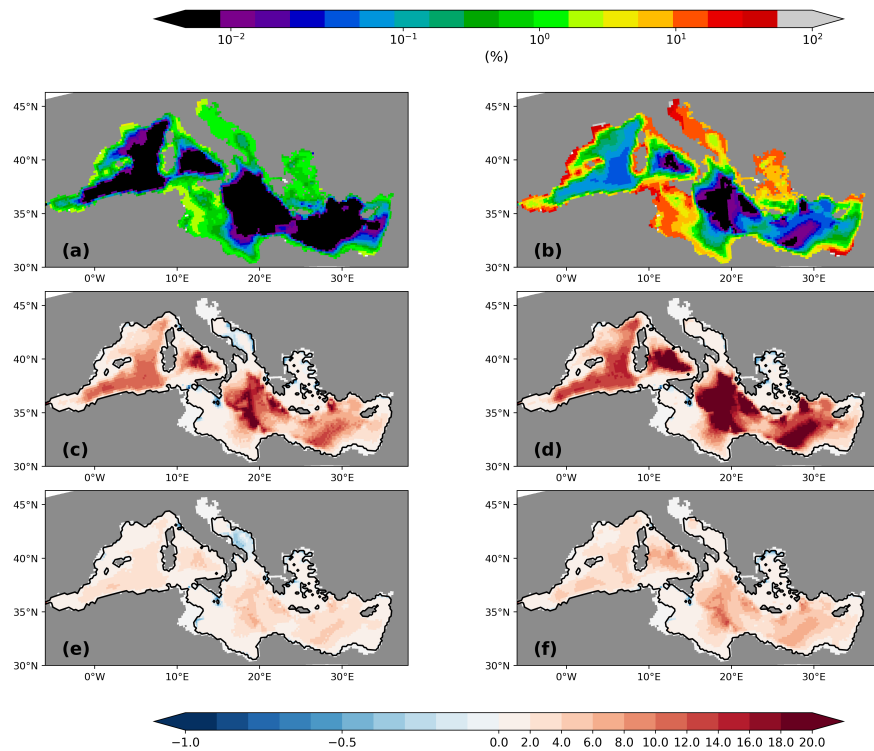
Figure 6. Weight-percentage sediment contribution in the upper 6 mm of the sediment column of detritus (a) and opal (b) for the PI of GLAC-1D (in %). Relative changes between LGM and the corresponding PI are given for detritus (c, e) and opal (d, f) for GLAC-1D (c, d) and ICE-6G (e, f). Note the logarithmic color scale for panels (a, b) above and the nonlinear color scale for (c, d, e, f) below the figure.

4 Changes in the patterns of the Last Glacial Maximum

4.1 Changes of the physical environment

The sea surface temperatures of the LGM in both simulations are generally about 4-8 K lower than for the PI (Fig. 7a, c) which is in line with paleo-temperature estimates (Hayes et al., 2005; Kuhlemann et al., 2008). The comparison to SST reconstructions from planktic formaminiferal assemblages (Hayes et al., 2005) shows that model biases are within the range of results for different reconstruction methods (Fig. 8, Fig. 9). Out of the parent simulations, GLAC-1D has a weaker Atlantic overturning circulation and a relatively colder climate over the North Atlantic than ICE-6G (Kapsch et al., 2022) which is reflected in the larger SST anomaly (and larger deviation from the reconstructions, Fig. 9) throughout the entire MedSea.

For the Gulf of Lions, the annual SST of the LGM is much higher in both simulations than in the reconstruction creating a larger deviation to the proxy data compared to the eastern basin (Fig. 8, Fig. 9). As the coarse resolution atmospheric parent models are missing the permanent ice cover over the Alps, the transport of cold air towards the gulf is potentially underrepresented in the summer season and causes this bias (Fig. A4).
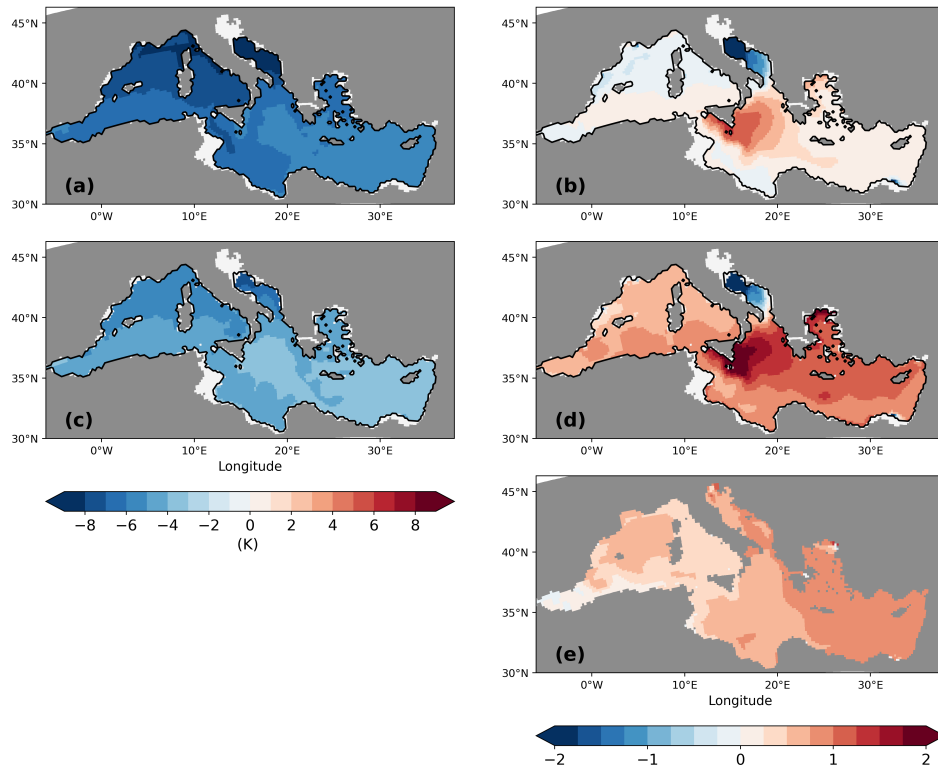
Figure 7. Anomalies of sea surface temperature (K) (a, c) and sea surface salinity (b, d) between LGM and PI for GLAC-1D (a, b) and ICE-6G (c, d). Panel (e) shows the anomaly of sea surface salinity between PI-Straits and PI of GLAC-1D. The anomaly of sea surface temperature between PI-Straits and PI of GLAC-1D is small (not shown).
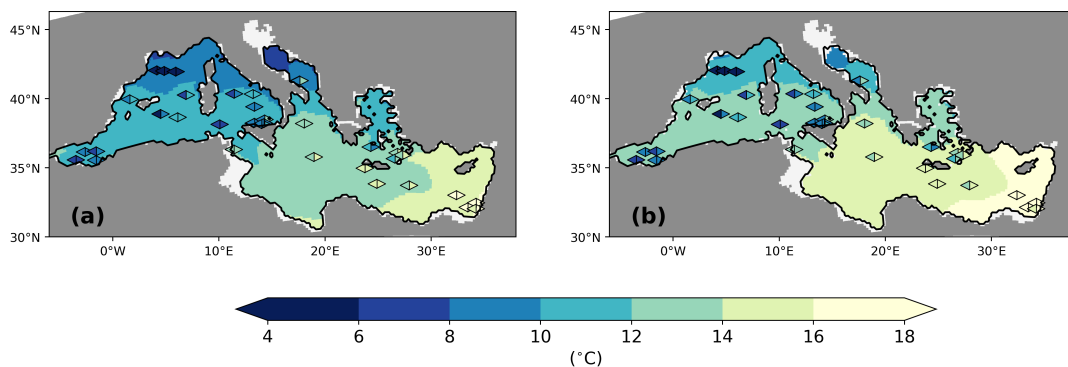
Figure 8. Annual mean sea surface temperature (°C) at the LGM for GLAC-1D (a) and ICE-6G (b). Overlaid data from Hayes et al. (2005) are estimates from two different methods: artificial neural network (left part of rhombus) and the revised analogue method (right part of rhombus). See Hayes et al. (2005) for more details.
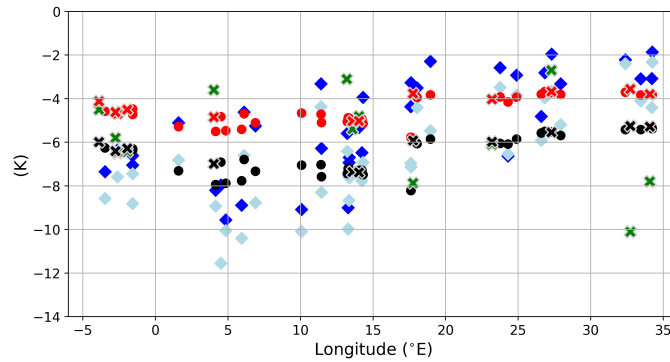
Figure 9. Annual mean SST differences between LGM and PI for GLAC-1D (black circles) and ICE-6G (red circles) against the longitude. Overlaid are the same SST data as in Fig. 8 using an artificial neural network (blue diamond) or the revised analogue method (light blue diamond), but here as deviation from modern SST ~~(World Ocean Atlas, Locarnini et al. (2018))~~(World Ocean Atlas, Locarnini et al., 2018). In addition, SST change estimates based on alkenones from Lee (2004) with updates from the PANGAEA database (Herbert et al., 2018; Rodrigo-Gámiz et al., 2014; Castañeda et al., 2010) are given (green ~~triangle~~crosses) with the corresponding SST difference for GLAC-1D (black crosses) and ICE-6G (red crosses). Units are in K.

We also find an intensification of the SST gradient between the eastern and western basin during the LGM as proposed by Hayes et al. (2005). Annual mean temperature differences between GOL and LEV rises from 2 K to about 4.5 K (Fig. 2). Sea surface salinity (SSS) changes show a very similar spatial pattern for both simulations with a higher SSS change in the eastern basin. GLAC-1D has a lower SSS increase than ICE-6G (Fig. 7b, d). This is partly due to a negative SSS anomaly at

280 the Strait of Gibraltar entrance (Fig. 7d). The water mass boundary of the subpolar gyre in the North Atlantic of the parent simulation of GLAC-1D shifts further to the south compared to ICE-6G during the LGM. Thus, in a colder GLAC-1D climate less saline subpolar water enters the Gulf of Cadiz and imprints on the SSS anomaly of the MedSea. The most pronounced increase in SSS is found in the Ionian Sea which is attributable to changes in the circulation linked to the freshening of the Adriatic Sea and the consequential strong reduction of local deep water formation (see ~~Fig. A2 for changes in the maximum~~

285 ~~mixed layer depth as indicator for deep water production~~discussion on pycnocline changes below). The modelling study by Mikolajewicz (2011) demonstrated a similar shift of the area of deep water formation from the Adriatic Sea to the Ionian Sea also accompanied by the largest SSS increase from present day to the LGM. In contrast to Mikolajewicz (2011), the Adriatic Sea keeps a weak anti-estuarine circulation during the LGM in our simulations.

SSS changes between LGM and present day based on δ^{18}O reconstructions from planktic foraminifera were estimated to

290 +1.2 (+2.7) in the western (eastern) basin (Thunell and Williams, 1989) which is about 1-1.5 higher than our results. However, these estimates come with an unclear uncertainty. The underlying method combines global δ^{18}O changes due to ice sheet growth ~~(1.2 °/₀₀ with a potential error of approx. 30 %, Schrag et al. (2002))~~(1.2 °/₀₀ with a potential error of approx. 30 %, Schrag et al., 2 , LGM temperature estimates from alkenone ratios ~~(uncertainty ±1.3 °C⁻¹, Sijinkumar et al. (2016))~~(uncertainty ±1.3 °C⁻¹, Sijinkumar e , and a global δ^{18}O-salinity slope regression (0.41 °/₀₀ psu⁻¹, Thunell and Williams (1989), 0.25-0.45 °/₀₀ psu⁻¹, Emeis et al.

(2000)). Sijinkumar et al. (2016) performed an error propagation for reconstructed LGM salinities in the Bay of Bengal and calculated an error range of 1.8-2.6 for salinity change estimates of 0.9-3.5 between LGM and the modern ocean. Given these large uncertainties in the SSS reconstruction, we cannot assess our model results based on these literature estimates. Our simulated SSS changes are at least consistent with the applied forcing. Besides the changing salinity in the Gulf of Cadiz, which is determined by the parent simulation, we find e.g. that the spatial SSS difference between the Levantine and the Gulf of Lions increases by 0.3 from the PI to the LGM in GLAC-1D (0.5 for ICE-6G) (Fig. 2). This is attributable to a longer residence time of the water within the basins due to a reduced zonal overturning ~~stream function~~ circulation (ZOC), which also means that the surface water is exposed to net evaporative fluxes for a longer time.

The ZOC of both experiments show that the strong, deep reaching anti-estuarine circulation (~~max~~ maximal transport of 1.2 Sv, vertical extension to 600-800 m) in the PI is reduced to 0.6 Sv and reaches only to 400 m depth in the LGM (Fig. 4). The reduction of the ZOC is linked to the change of the outflow at the Strait of Gibraltar due to lower sill depth (Fig. 3, Table 1), changed freshwater budget (Table 2), and a concurrent increase of the salinity gradient between surface and intermediate layers (0.17-0.265 between 466 m and surface, Fig. 2). The magnitude of the simulated ZOC reduction fits well to the previous estimates of 40-65 % from modelling studies (Myers et al., 1998; Mikolajewicz, 2011) and theoretical considerations ~~(Rohling (1991) and refs within)~~(Rohling, 1991, and refs within). About two-third of the ZOC reduction can be attributed to a reduced cross-sectional area ~~at~~ of the Strait of Gibraltar as demonstrated by the sensitivity study PI-Straits (Fig. 3 and its zonal stream function in the appendix, Fig. A1).

To gain more insight into the combined effects of LGM changes in SST, SSS and ZOC on the circulation, we investigate the depth change of the pycnocline in February, when a shallower winter pycnocline depth could allow for a higher nutrient supply to the productive surface layers as postulated by Rohling (1991). The pycnocline depth in February for the PI of both experiments is very similar as a consequence of the similarity of the parent simulations for PI. ~~Fig.~~ Figure 10 shows, therefore, only the result of the PI for GLAC-1D. For the LGM, we see a shallowing of the pycnocline by 20-60 m for most areas of the MedSea in both simulations. This corresponds to a relative shallowing to about 65-85 % between the LGM and the PI, which is similar to the estimate of Rohling (1991) and is in line with his theoretical approach. In regions of deep water formation in the PI (i.e. the Gulf of Lions, the Adriatic Sea, Fig. A2), the shallowing is more pronounced (> 60 m) due to an increased water column stability. Only the northern Ionian Sea shows a strong deepening of the pycnocline for the LGM, which is linked to the lack of deep water formation in the Adriatic Sea (Fig. A2). During the PI, dense water is formed in the Adriatic Sea, flows across the Otranto sill, supplies to the deep and intermediate water of the Northern Ionian Sea, and, thus, lifts up the density ~~iso-surfaces~~ isosurfaces (Liu et al., 2021). This deep water formation during the PI leaves its imprint on the water masses of the northern Ionian Sea where colder, less saltier and "younger" water mass properties are found at intermediate water depths in the west of the Ionian basin compared to the east (not shown). At the LGM, water mass properties are very similar across the entire northern Ionian basin and, thus, we find a deepening of the pycnocline primarily along the eastern side of the Ionian basin. In the sensitivity study PI-Straits, the deep water formation in the Adriatic Sea is slightly reduced, but still active (Fig. A2~~e~~c), and, hence, we do not find a corresponding pattern in the pycnocline depth change (Fig. 10). The similarity of the spatial pattern in PI-Straits compared to the LGM simulations underlines that shallower sill depths alone are the largest contributor
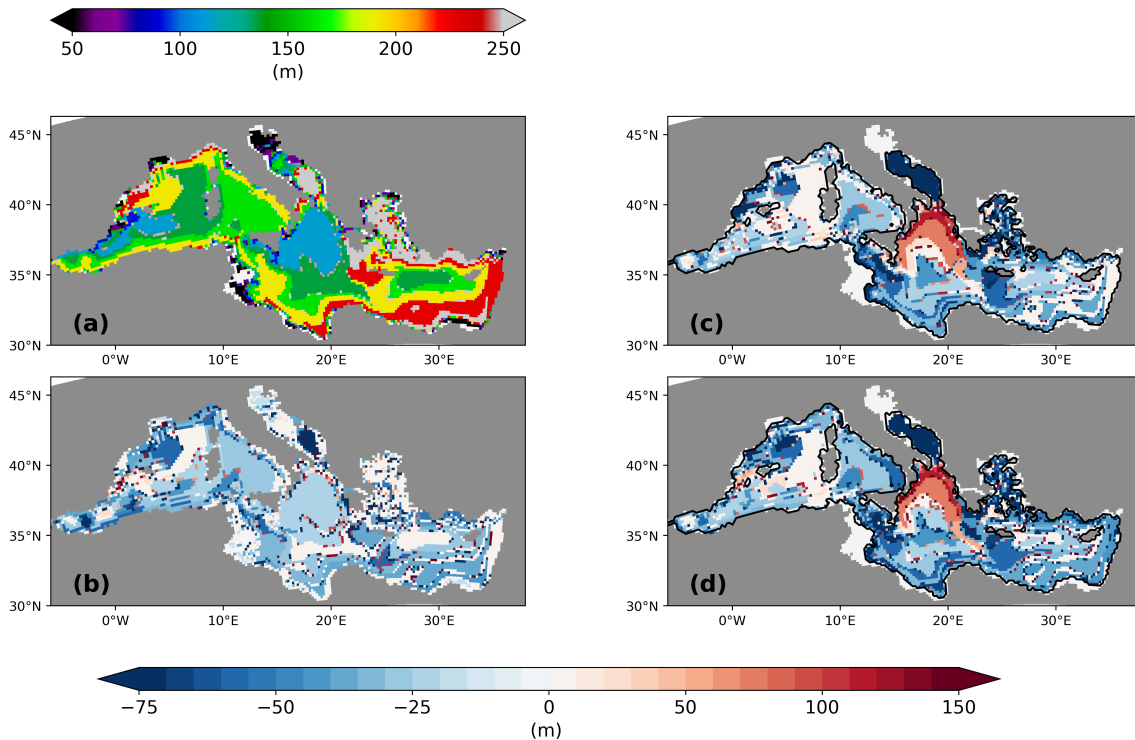
Figure 10. Depth of pycnocline in February for PI of GLAC-1D (a) and the pycnocline depth change between LGM and PI for GLAC-1D(b) and ICE-6G (d). Panel (b) gives the pycnocline depth change between PI-Straits and the PI of GLAC-1D. Units are in (m).

330 to the pycnocline anomaly for most areas of the MedSea. The reduced ZOC (Fig. 3) and the consequentially longer water residence time within the basins of the MedSea increases the SSS (Fig. 7) and intensifies the water column stratification in all experiments with LGM sill depth (Fig. 2b, f).

4.2   Changes of the biogeochemical distributions in the water column

Following the argument by Rohling (1991), who postulated that a shallower pycnocline provides more nutrients to the produc-
335 tion zone and enlarges the NPP, we might expect, according to Fig. 10, an increase in surface phosphate concentration and NPP. In contrast, the simulated surface phosphate concentration at the LGM decreases remarkably by ~~20 to 60~~ 20-60 % compared to its PI value (Fig. 11b, d). Consequentially, the vertical integrated net primary production resembles this pattern change (Fig. 5c, e). Largest changes in surface phosphate and NPP are located in deep water formation areas and the western Ionian Sea. Suppressed or shallower deep water formation hampers the supply of phosphate (PO4) to surface layers. Relative increases of
340 surface phosphate are found only in the Alboran Sea and in vicinity of rivers. The increased river runoff during the LGM (~~Tab.~~ Table 2) also transports more nutrients (phosphate, nitrate, silicate) to the MedSea according to our parametrization which is based on a basin-wide fixed river nutrient concentration times river discharge. The relative increase in NPP in the vicinity of
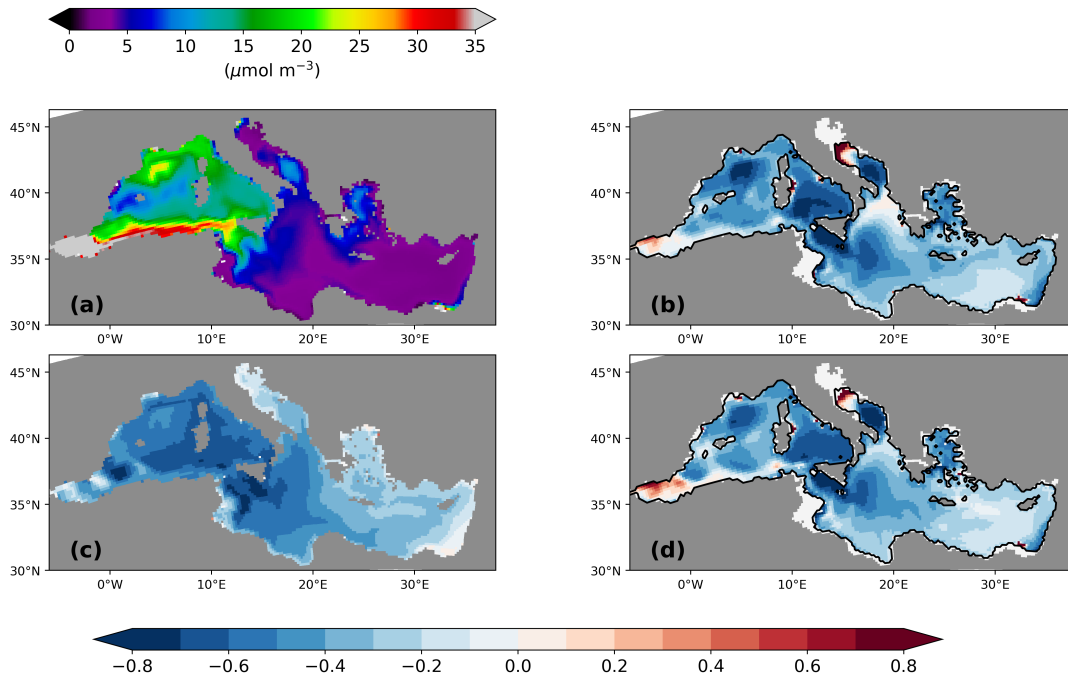
Figure 11. Surface phosphate concentration (μmol P m^{-3}) for the PI of GLAC-1D (a, see color scale above panel a) and its relative concentration change between the LGM and the PI for GLAC-1D (b), and for ICE-6G (d). Panel (c) shows the relative concentration change between PI-Straits and the PI of GLAC-1D.

the Nile river underlines the change in the runoff (Fig. 5c, d). In the northern Adriatic Sea, we see a relocation of the productive area. Bathymetry changes due to the low sea level stand move the coast line and, thus, the river estuaries towards the south.

345 Note, that we find a similar overall relative decrease of surface PO4 for PI-Straits, only missing the extreme changes in deep water formation areas and the northern Adriatic Sea (Fig. 11c).

Besides an overall decrease to the annual mean NPP, we also find a flattening of the seasonality of the production. To illustrate the changes of the NPP seasonality, we define the peakiness of the seasonal NPP with

$$P = \frac{12 \, NPP_{max}}{\sum NPP_{ann}}$$

350 where NPP_{max} is the annual maximum of the monthly mean NPP (we use a running mean of two months to ensure that we find a correct maximum within our monthly mean data), and $\sum NPP_{ann}$ is the total annual NPP. In case of the same NPP for each month, P would be exactly 1. For P=3, 50 % of the annual NPP is confined to two adjacent months. For the theoretical case of P=6, 100 % of the annual NPP would occur in two adjacent months. The peakiness is, thus, a simple measure to characterize "blooming areas" and "non-blooming areas", independent of the annual mean NPP ~~(see a similar approach~~

355 ~~by D'Ortenzio and Ribera d'Alcalà (2009))~~(see a similar approach by D'Ortenzio and Ribera d'Alcalà, 2009). For the PI, the peakiness is close to 3 in the Aegean and the northern Levantine and well above 2.2 for the Gulf of Lions and large parts of the Levantine indicating a well developed seasonal peak in the production, primarily in spring, and a lower production throughout
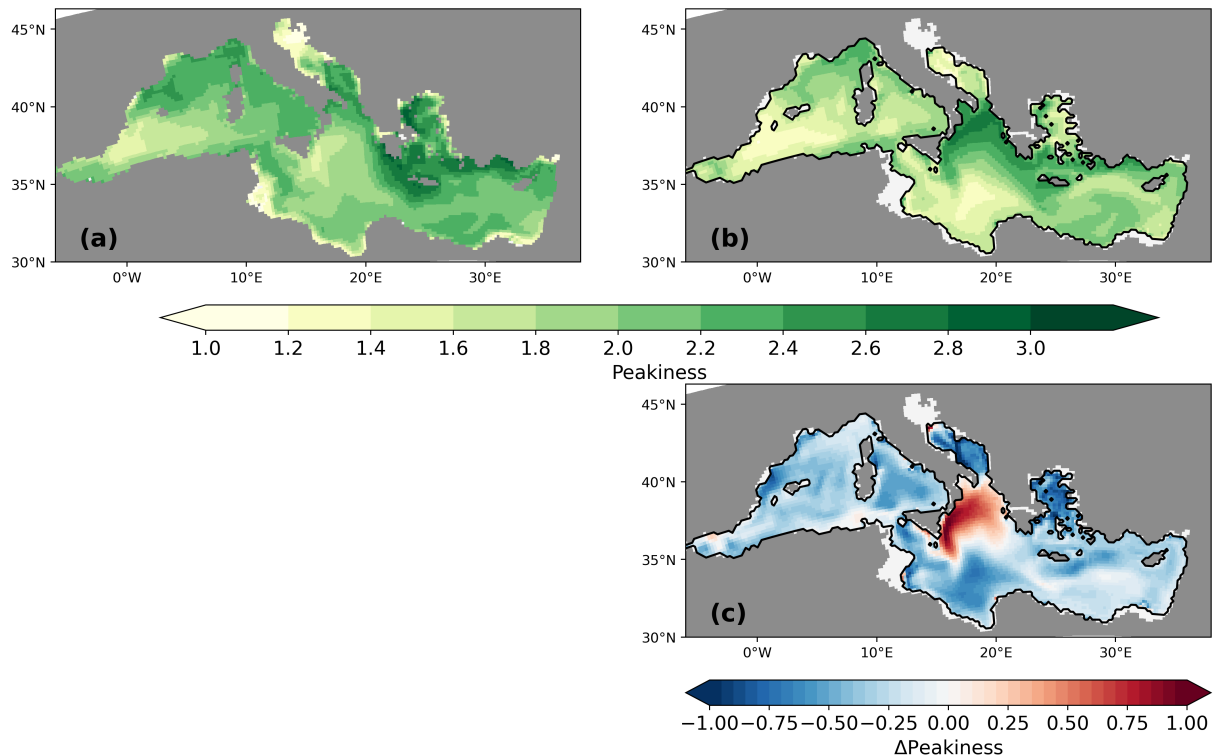
Figure 12. Peakiness P for the PI (a) and the LGM (b) of GLAC-1D and the difference between LGM and PI of P. See text for definition of peakiness.

the rest of the year (Fig. 12). Coastal areas, especially in the vicinity of rivers show a more uniform production seasonality (P close to 1). This pattern for the PI resembles the findings of D'Ortenzio and Ribera d'Alcalà (2009) who characterized the

360 seasonal cycle of surface biomass for different areas of the MedSea based on satellite data. For the LGM, the seasonality of the NPP flattens throughout the entire MedSea. The northern Ionian Sea is the only exception, where we find a shift towards blooming conditions. The pattern change of the peakiness resembles the changes of the pycnocline (Fig. 10), which might explain the changes in the nutrient supply throughout the year.

To understand the fate of the surface nutrients, we first look at the vertical PO4 distribution. As already visible in the concen-

365 tration profiles for the GOL and the LEV (Fig. 2), we see a strong accumulation of PO4 below 100 m during the LGM. The east-west cross-section through the MedSea displays sharp vertical gradients around 100 m with relative changes of more than 100 % in both basins and both LGM simulations (Fig. 13). In PI-Straits, an accumulation of PO4 at depth is missing and we rather find a nutrient depletion over the entire MedSea. The shallower sill depths in the LGM and PI-Straits lead not only to a more sluggish overturning circulation (Fig. 4), but also to a shift of the centre of maximum zonal transport to a shallower depth.

370 This causes a very effective lateral export of nutrients and organic material at intermediate depth from the eastern to the western basin and out of the MedSea and, thus, leads to the depletion of nutrients in PI-Straits. In the LGM simulations, the same
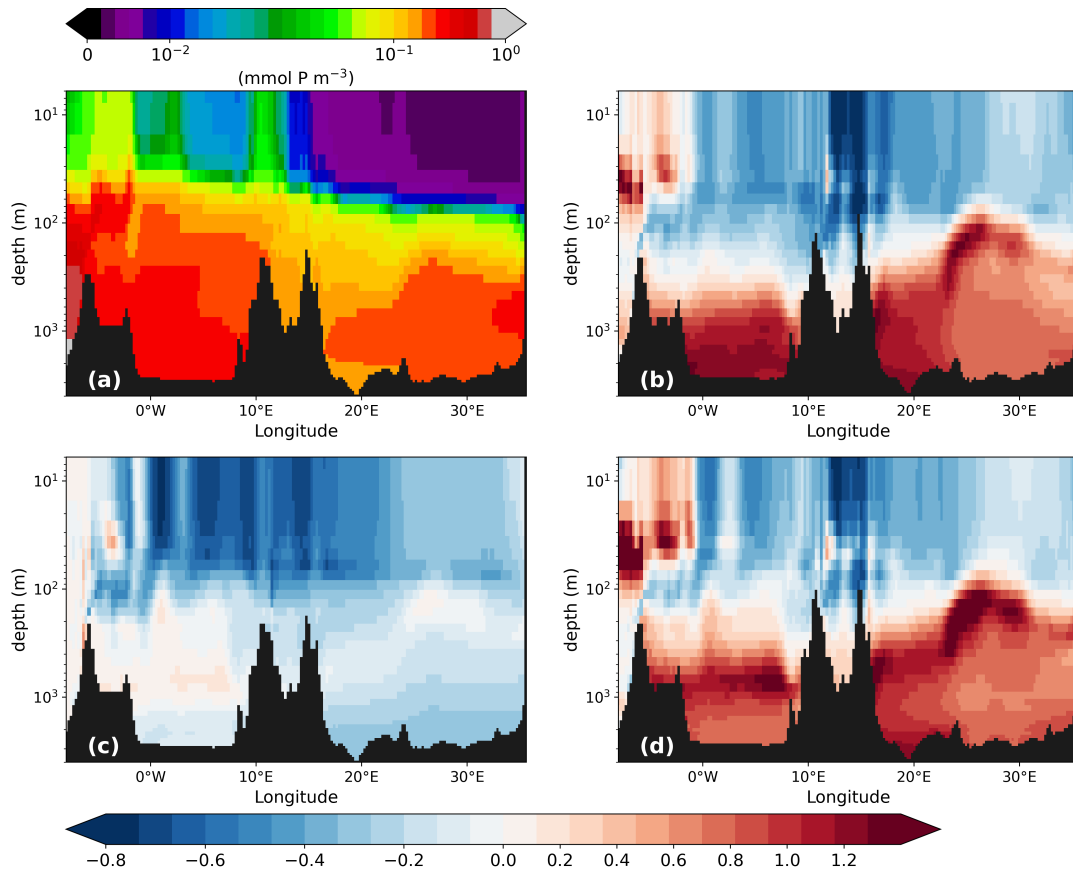
Figure 13. Phosphate concentration (mmol P m^{-3}) along the east-west transect (for location see Fig. 1) of the PI of GLAC-1D (a) and the relative concentration change between the LGM and the corresponding PI of GLAC-1D (b) and ICE-6G (d), and between PI-Straits and the PI of GLAC-1D (c). Note the logarithmic color scale in panel a) and the logarithmic depth scale in all panels.

process is active, but is overcompensated by the effect of an additional change of the remineralization rate of organic material. The remineralisation rate depends primarily on temperature and oxygen availability. Any potential restrictions by oxygen are negligible in the well ventilated water of the MedSea during the PI and the LGM (Fig. 2, Fig. A5). Temperatures at the LGM are significantly lower by -8 to -4 K than in the PI (Fig. 2), causing remineralization rates to drop to 51-64 % of the PI values, respectively. In combination with gravitational sinking, more detritus reach intermediate and deep layers and potentially enter the sediment in the LGM simulations. The transfer efficiency of detritus T_{eff} (Weber et al., 2016) which relates the detritus sinking flux at 1000 m to that of 100 m illustrates this effect of the remineralisation rate (Fig. 14).

In the PI, less than 10 % of the detritus export flux at 100 m reaches the 1000 m depth level. This is also true for PI-Straits which has a nearly identical vertical temperature distribution as the corresponding PI simulation (differences of less than ±0.5 K between PI-Straits and PI of GLAC-1D, not shown). In contrast, T_{eff} increases to 14-28 % in both LGM simulations. Higher T_{eff} in the LGM of GLAC-1D than in ICE-6G is attributable to the overall colder conditions in this simulation (Fig. 2, Fig.
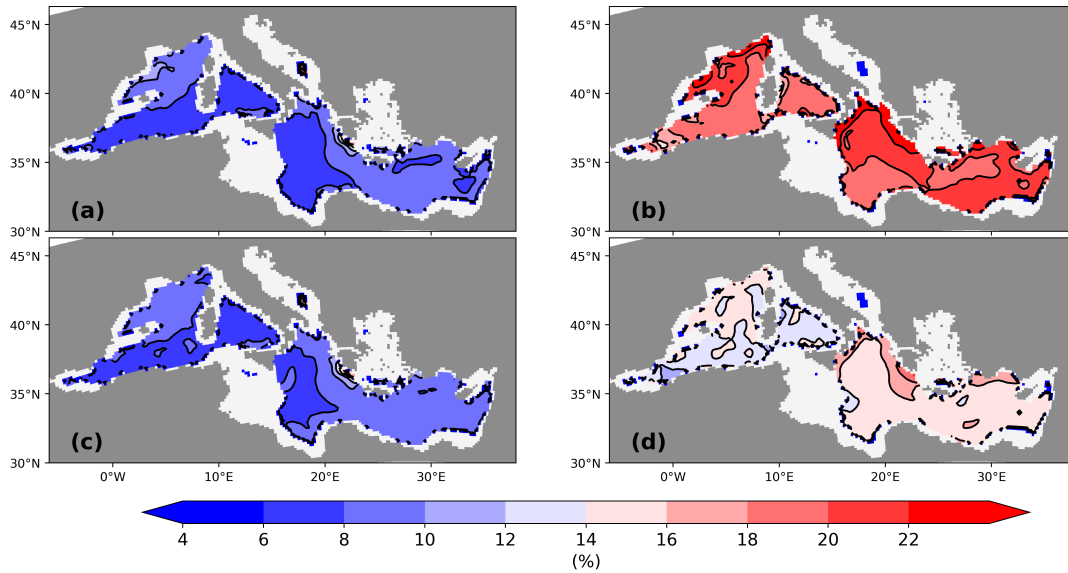
Figure 14. Transfer efficiency of detritus calculated as ratio of the detritus flux at 1000 m to 100 m on a percentage basis (%) for the PI of GLAC-1D (a) and for the LGM of GLAC-1D (b) and ICE-6G (d). Panel (c) gives the transfer efficiency for PI-Straits.
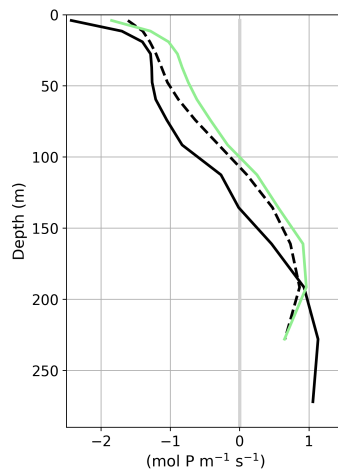
Figure 15. Vertical depth profile of the meridional transport of the sum of dissolved and organically bound phosphate (mol P m^{-1} s^{-1}). over the Strait of Sicily for the PI (solid black line), the LGM (dashed black line) of GLAC-1D and PI-Straits (solid green line). Positive values indicate northward transport, i.e. from the eastern into the western basin of the MedSea.

7). To further illustrate the combined effects of shallower sill depths and colder temperatures on the nutrient distribution, we present, as an example, the dynamical conditions in the Strait of Sicily for GLAC-1D (Fig. 15). The mean transport of total

385   phosphate (i.e. the sum of dissolved and organically bound phosphate) across the strait is southward in the upper 137 m for the

PI, with a corresponding northward return flow below. With the shallower strait depths for GLAC-1D-LGM and PI-Straits, the interbasin exchange fluxes are, as expected, reduced and the neutral position between the baroclinic flow components shifts to 111 m and 97 m, respectively. Below this depth, both simulations show a more effective export of total phosphate from the eastern basin as compared to GLAC-1D-PI. In combination with a reduced inflow of total phosphate into the eastern basin, this leads to the simulated nutrient depletion in the upper 200 m of the water column as seen in Fig. 13. The warmer temperatures in PI-Straits than in the GLAC-1D-LGM allow for a higher biological production despite similar near-surface phosphate concentration, as indicated by slightly higher organically bound phosphate concentration in the upper ocean (Fig. A6b). However, the temperature effect on remineralization manifests in a more rapid decay of detritus and a higher phosphate concentration between 100-200 m in PI-Straits compared to the LGM simulation of GLAC-1D (Fig. A6a), eventually leading to the even larger nutrient depletion of the upper ocean.

In brief, the impact of shallower sill depths is primarily a shallowing of the overturning circulation which leads to a more effective zonal export of nutrients from intermediate ocean depths. As seen for PI-Straits, the phosphate inventory of the entire MedSea consequently decreases even under present day climate conditions. Furthermore, a potential increase in net primary production due to a shallower pycnocline, as proposed by Rohling (1991), is outweighed by this efficient drainage of nutrient from the MedSea. For the colder LGM conditions, we find a comparable decrease in surface PO4 concentrations (Fig. 5) and NPP (Fig. 13), but temperature-induced lowering of remineralization rates leads to a higher T_{eff} and a phosphate accumulation at greater depths. It is important to emphasise that a higher T_{eff} during the LGM masks the signal of the lower surface net primary production and leaves its imprint in the sediment. The implications will be discussed in the next section.

4.3   Changes in the sediment composition for the LGM

As mentioned, changes in the remineralisation rate also modify the deposition flux to the sediment. Relative changes of the settling flux rate, especially in the deep Ionian Sea, are 5-10 times higher than during the PI, while NPP decreases to -0.4 to -0.6 in the same area (Fig. 5). Fig. Note, that increased deposition fluxes increase the abundance of benthic foramifera in the real world which is observed for several sediment cores from the eastern basin with a mean relative change of the benthic foraminiferal number of about 7 (range of 0.1 to 30.2, Schmiedl et al., 2010, 2023, and references therein). Hence, our simulated changes in organic matter deposition agree, to first order, with observed indicators. Figure 6 displays the changes in weight-percentage sediment composition between the LGM and the PI. Both LGM simulations show an increased fraction of detritus and opal in the upper 6 mm of the sediment column (first two model layers of the simulated sediment column) with at least a doubling of the local contribution of both components almost over the entire MedSea. Changes in the deep basins are more pronounced due to the higher transfer efficiency at the LGM (factor of ten). Again, the even higher transfer efficiency due to colder temperatures of GLADC-1D is evident from the larger fractional change in detritus and opal. The calcite fraction correspondingly decreases throughout the MedSea with largest changes in the Ionian Sea and the Adriatic Sea (< 0.5) and more moderate changes in the Alboran Sea (Fig. A3). Sediment core data confirm 20-50% % lower than modern carbonate contents during the LGM for different areas of the Mediterranean Sea (Aksu et al., 1995; Hoogakker et al., 2004). Please note, that in

420   our simulation a large part of the weight-percentage change in calcite is related to the higher dust deposition during the LGM, especially in the northern part of the MedSea (Fig A3, Albani et al. (2016)).

Higher accumulation of organic carbon during the LGM as compared to the PI is supported by an increased abundance of benthic foraminiferal tests which develops under elevated food supply of detritus ~~(Schmiedl et al. (2010) and refs. within)~~(Schmiedl et al., 2). Hence, our simulated sediment changes are in good agreement with sediment proxies. Moreover, it has to be emphasized that

425   these elevated sedimentary fluxes occur under a simulated lower NPP. Thus, our results link the supposedly contradictory statements of a higher NPP during the LGM as inferred from benthic proxy data (Schmiedl et al., 2010) and a lower NPP as derived from the absence of small placoliths, a coccolithophoridae used as classical indicator for high nutrient availability (Ausín et al., 2015).

4.4   Assessment of the biological production temperature T_{org}

430   The use of the alkenone unsaturation ratio $U_{37}^{K'}$ to estimate the annual mean sea surface temperature is a widely applied paleoceanographic tool (Müller et al., 1998; Conte et al., 2006). Potential seasonal biases which arise from the marked seasonality in the abundance of primary producers and the link between primary production and surface ocean temperatures, have been a debatable issue, but, for most of the ocean regions, Rosell-Melé and Prahl (2013) concluded that "the integrated sedimentation patterns for $U_{37}^{K'}$ measured in sediment trap time series provide a measure of annual mean SST" and that a seasonal pattern is

435   not apparent in a temperature reconstruction with $U_{37}^{K'}$ in a global application. However, all derived relationships for $U_{37}^{K'}$ are based on modern conditions of spatial and temporal surface ocean temperature pattern, as well as, on present day variations in biological production. So far, there are no data or methods to assess these relationships for past climate conditions.

Our diagnostic tracer T_{org} (see Sec.2) mimics the information which is obtainable from alkenones without the methodological and physiological uncertainties typical of alkenone undersaturation estimates (Conte et al., 2006). Thus, T_{org} gives

440   us the opportunity to analyse, i) how well it captures the surface ocean temperature change between past and present, and ii) which processes might contribute to the difference of the signals between T_{org} and temperature. To tackle these questions, we calculate the change in T_{org} between LGM and PI of GLAC-1D (ΔT_{org}) and the corresponding change in the surface ocean temperature, for which we use the annual mean temperature of the upper 32 m (ΔT_{32}, i.e. corresponding to the first 4 layers of our model), where most of the simulated biological production takes place.

445   ~~Fig.~~Figure 16a shows the difference of ΔT_{org} and ΔT_{32}. Note, that we here discuss only the analysis for GLAC-1D. The corresponding figure for ICE-6G is given in the appendix for the sake of completeness (Fig. A7). For most parts of the MedSea, the cooling signal that is captured by ΔT_{org} is smaller than ΔT_{32}, resulting in an absolute positive difference because both anomalies are negative. In the western MedSea, the absolute value of ΔT_{org} underestimates that of ΔT_{32} by 0.4-1 K, and even higher differences are found in a selected areas, e.g. the Adriatic Sea and close to the shelf regions in the western Ionian Sea.

450   Our result indicates that T_{org} does not just simply reflect T_{32}, but that additional processes must shape T_{org}. This might be the seasonality of the net primary production or processes within the water column such as the remineralization of organic matter during settling. The latter was postulated by Conte et al. (2006) who showed that different remineralization functions alone led to changes of T_{org} between 0.4-0.9 K in their hypothetical case studies.
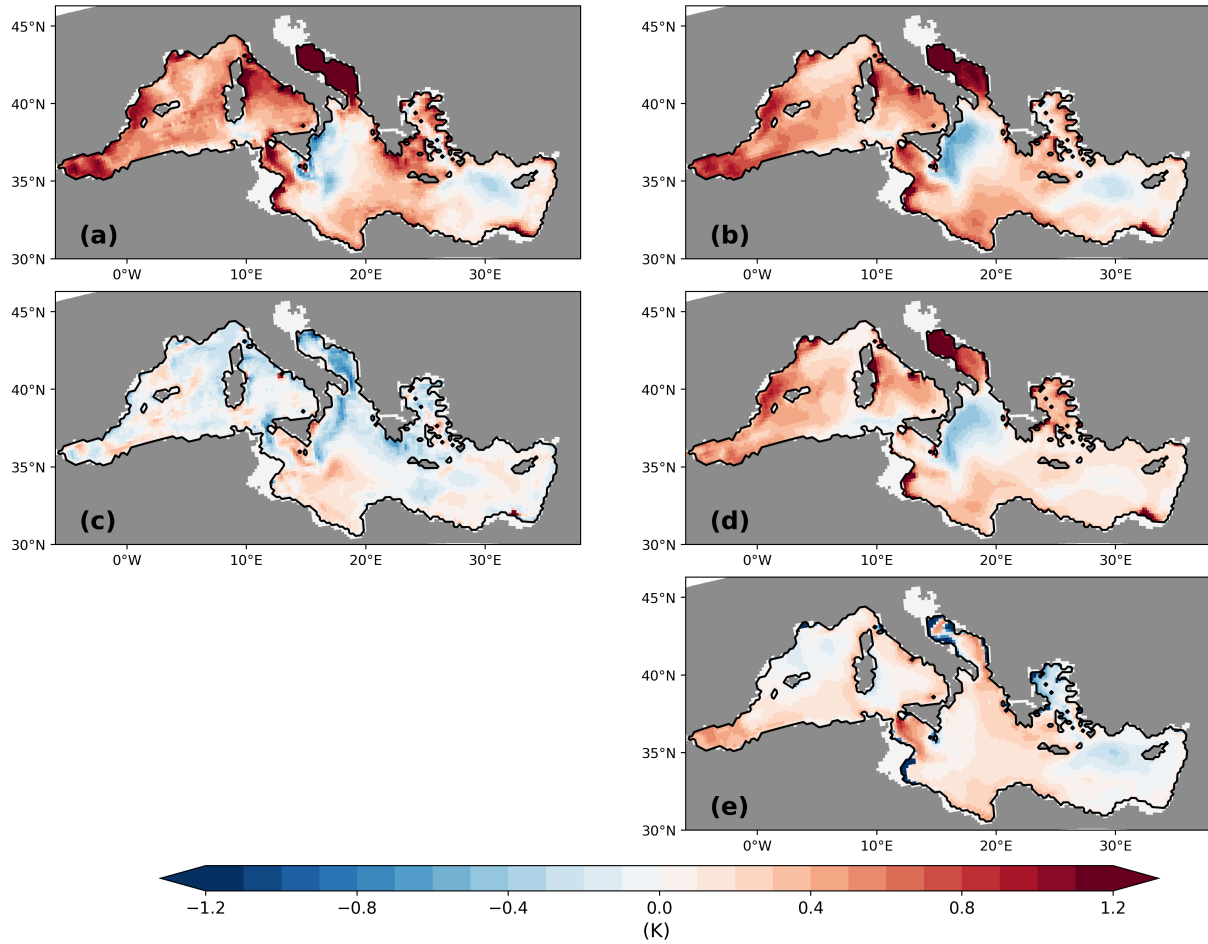
Figure 16. Difference of ΔT_{org} and ΔT_{32} (a). Note, that both anomalies are negative; thus, positive values in (a) indicate a larger absolute ΔT_{32}. Also shown is the difference of ΔPWT and ΔT_{32} (b) and the difference between ΔPWT and ΔT_{org} (c). Panel (d) shows ΔPWT_{NPP}, the NPP related contribution to ΔPWT, and panel (e) displays ΔPWT_T - ΔT_{32}, the temperature related contribution. All units are in (K). See text for definitions.

To gain insight into the drivers of T_{org}, we construct a diagnostic production-weighted temperature (PWT) by integrating the product of the monthly mean NPP and the monthly mean temperature over all layers and all months and dividing the result by the vertical integrated annual NPP. The difference between PWT for the LGM and the PI (ΔPWT) reflects changes in the NPP and its temperature recording without any impact from remineralization or settling processes. We find a strong similarity between the patterns of the difference of (ΔPWT -ΔT_{32}) and (ΔT_{org}-ΔT_{32}), which underlines that changes in the surface conditions are the major drivers of T_{org} variations (Fig. 16a, b). This becomes even more obvious when we separate the variations of ΔPWT into a part attributed to variations in the NPP (ΔPWT$_{NPP}$) and a part attributed to temperature variations (ΔPWT$_T$). For ΔPWT$_{NPP}$, we calculate the difference of the present day temperature times the monthly mean NPP of the LGM and the present day temperature times the monthly mean NPP of the PI. Thus, we get variations based only on the shift of the NPP seasonality, which results in a changed sampling of the monthly mean temperatures. For calculating ΔPWT$_T$, we use the present day NPP times LGM temperatures and present day NPP times PI temperatures. This gives the contribution from the fact that the annual mean LGM cooling signal is not distributed uniformly over the year. In our GLAC-1D simulation, the Levantine shows a stronger cooling signal than the annual average during February to April, while in the Ionian Sea, the temperatures of July to September primarily contribute to the annual mean LGM cooling signal (not shown).

~~Fig.~~ Figure 16d shows that the pattern of ΔPWT$_{NPP}$ explains most of the signal found in ΔPWT, including the cooling signal in the northern Ionian Sea. Furthermore, ΔPWT$_{NPP}$ resembles the pattern of the peakiness change (Fig. 12) with a warming signal in regions with decreasing peakiness and vice versa. This clearly indicates that the NPP driven part is the major driver of PWT changes. The temperatures related part ΔPWT$_T$ has a minor contribution to ΔPWT (Fig. 16e), but it explains e.g. the small cooling signal west of Cyprus. As mentioned before, the absolute spring temperature change in the Levantine is stronger than the annual mean LGM cooling signal. Other potential sampling biases, such as vertical shifts in the production or due to sampling over shallower water depth in the LGM, have no impact on ΔPWT (not shown). The contribution from processes within the water column, e.g remineralization or lateral advection, are estimated by the difference between ΔPWT and ΔT_{org} (Fig. 16c). For most of the MedSea, this contribution is rather small, except for regions where we also find strong changes in the physical ocean, such as the northern Ionian Sea, the Adriatic Sea, or the Strait of Sicily. A similar pattern for ΔPWT-ΔT_{org} is seen for ICE-6G (Fig. A7c). We ~~can not~~ cannot disentangle whether the cause of this signal in T_{org} is related to the lateral advection of organic material from distant production regions or a temperature-induced remineralization change or the combination to both.

To summarize, we find that the recorded temperature of ΔT_{org} underestimates the climate signal which is represented by ΔT_{32}. The shift in the seasonality of the NPP between past and present is a main driver of the difference between ΔT_{org} and ΔT_{32}, as a more uniform seasonal cycle in NPP tends to sample the relative warmer temperatures of late spring and summer. Despite the simplicity of our artificial temperature tracer T_{org}, our simulations might point to the methodological problem of using present day derived correlations for paleo-records. Furthermore, local changes in the biogeochemical patterns increase the uncertainty that is intrinsic to the method (Conte et al., 2006).

5   Summary and ~~Discussion~~discussion

We apply a regional physical-biogeochemical ocean model of the Mediterranean Sea to investigate the biogeochemical state during the LGM. The use of a novel set of atmospheric and oceanic boundary conditions derived from paleo-simulations over 26,000 years with an Earth system model ~~(MPIESM, Kapsch et al. (2022))~~ (MPIESM, Kapsch et al., 2022) allows for running consistent time slice simulations for the LGM and the PI. To address uncertainties for the LGM, we take forcing data from two MPIESM runs based on different ice sheet reconstructions (Tarasov et al., 2012; Peltier et al., 2015). The computational efficiency of our calculations enables transient model simulations over 2000 years, which minimizes model drift and permits to attribute the simulated changes to physical and biogeochemical variations during the LGM. Our analysis is supported by a sensitivity study with present day climate and LGM strait bathymetry (PI-Straits) to disentangle topography driven and climate induced changes on the biogeochemistry.

Simulated circulation changes for the LGM are primarily caused by sea level low stands which lead to a weakening of the zonal overturning circulation and an intensification of water column stability. Our model results for the PI and the LGM are in line with previous ocean modelling attempts (Myers et al., 1998; Mikolajewicz, 2011; Sevault et al., 2014; Grimm et al., 2015) and theoretical considerations (Rohling et al., 2015). Simulated changes in sea surface temperature fall into the range of estimated surface cooling (Hayes et al., 2005).

The similarly strong response of the biogeochemistry in both LGM simulations indicates the robustness of the signals such as the nutrient accumulation below 100 m in the western and eastern basin of the MedSea. A quantitative evaluation of our simulated LGM distributions is still challenging. The evaluation of our results on the changes in the biogeochemistry during the LGM is restricted to the comparison to sediment core data, as to our knowledge there is no other published modelling study for the MedSea on this topic. As deduced from the sediment archives, an observed increase in diversity and the proportion of infaunal benthic foraminifera supports a glacial increase of organic matter fluxes to the sea floor (Schmiedl et al., 1998; Kuhnt et al., 2007; Abu-Zied et al., 2008; Schmiedl et al., 2010). Our model simulations confirm a higher detritus deposition, but this emerges from lower surface net primary production. Nutrient availability at the surface is reduced due to higher water column stability, a more efficient lateral nutrient export at mid-depth out of the MedSea, and a larger transfer efficiency of detritus at 1000 m under the cold LGM climate. A simulated lower production during the LGM is in agreement with data of sediment composition which show an absence of small placoliths, a coccolithophoridae used as classical indicator for high nutrient availability (Ausín et al., 2015). The occurrence of higher depositional fluxes despite lower primary production may clarify supposed inconsistencies in the interpretation of sediment data.

Our results emphasize the non-linearity of the response of the biogeochemistry to the hydrodynamical changes at low sea level stand. The assumption that the shallowing of the pycnocline inevitably introduces higher net primary production (Rohling, 1991) must be revised, and the interplay of altered lateral transport and reduced biological turnover rates must be considered for the LGM. This is underlined by the findings from the sensitivity experiment PI-Straits. By only reducing the water inflow from the Atlantic due to a shallower sill depth, most of the biogeochemical pattern change in the upper ocean, which is found for the LGM, is reproduced under present day climate. Our findings clearly point to the need of long-term modelling attempts,

ideally with a suite of different ocean biogeochemistry models, to gain further insights into the mean state and the temporal variations of the last glacial.

A noteworthy additional outcome of our simulations is provided by the artificial temperature tracer T_{org}. Changes in temperature of the upper 32 m between LGM and PI are imprinted on the sediment with a spatial heterogeneous pattern. In the western Mediterranean Sea, the T_{org} signal underestimates the LGM upper ocean temperature anomaly by about 1 K, while T_{org} records a stronger cooling of up to 0.5 K for the northern Ionian Sea. Thus, even within our ideal model world where all physiological and methodological uncertainties of temperature recording by planktic organisms (Conte et al., 2006) are omitted, the T_{org} signal captures the upper ocean temperature with a large uncertainty. Please note, that we do not claim that we correctly represent alkenone production, but we simply track the temperature at phytoplankton growth and the fate of the signal carried by organic material on its way to the sediment.

The newly developed model framework is here used to understand the biogeochemical state of the Mediterranean Sea at the LGM. The resulting distributions will serve as starting points for simulations covering the entire last deglaciation to present, with a main focus on the formation of sapropels in the eastern Mediterranean Sea during the early Holocene. As has been shown by time slice simulations (Grimm et al., 2015), the occurrence of sapropels does not depend only on "short-term" variations of biogeochemical and hydrodynamical conditions, but requires a long prelude of deep-water stagnation. Our new model framework in combination with the consistent forcing data sets from the MPIESM (Kapsch et al., 2022) provide a good working tool to tackle this topic.

Code and data availability. Model data and Python scripts used for the analysis and visualization are available on Zenodo (Six, 2024). Proxy data must be requested directly from Hayes et al. (2005), Schmiedl et al. (2010, 2023) or via the PANGAEA data base (https://www.pangaea.de/). Model code of medHAMOCC is available upon request from the corresponding author.

Appendix A: Additional ~~Figures~~ information and figures for GLAC-1D, ICE-6G, and ~~PI-straits~~PI-Straits

Region	GLAC-1D	ICE-6G	SAT1	RegCM-ES	other model studies
Alboran Sea	122	112	105	120± 38	24 -274
Balearic[a]	78	71	78-80		
Gulf of Lions	67	58	97		
Ligurian Sea	59	52	80		
Tyrrhenian Sea	66	60	67	128± 14	92-152
Adriatic Sea	30	22	71		
Ionian Sea	43	39	61-63	121 ± 15	27-153
Levantine	30	28	59-60	111 ± 18	36-158

[a] Balearic stands here for three regions: Balearic Sea, Algerian Basin and Algero-Provencal Basin

Table A1. Net primary production (in gC m^{-2} yr^{-1}) for the "Classic" Mediterranean Regions (e.g. see Bosc et al., 2004) from the PI of GLAC-1D and ICE-6G, satellite derived estimates SAT1 (Uitz et al., 2012), RegCM-ES (Reale et al., 2020), and a range of results from other model studies, all listed in Reale et al. (2020).
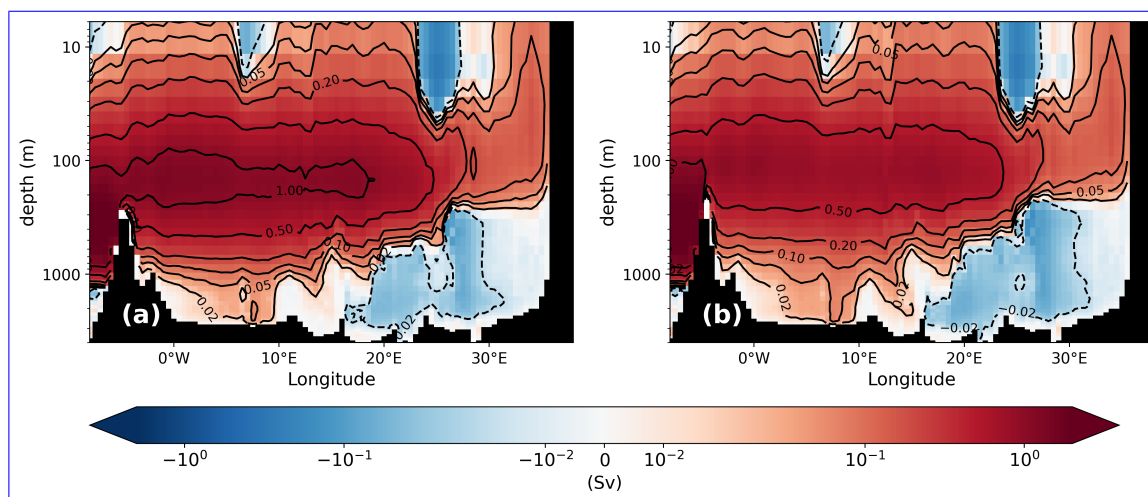
Figure A1. Mean zonal stream function (Sv) of PI of GLAC-1D (a, identical to Fig. 4a), just shown again for easier comparison) and PI-Straits (b). Contour lines are given as dashed line for (-0.02), and as solid lines for (0.02), (0.05), (0.1), (0.2), (0.5), and (1.0). Please note the logarithmic depth scale and the logarithmic color scale.
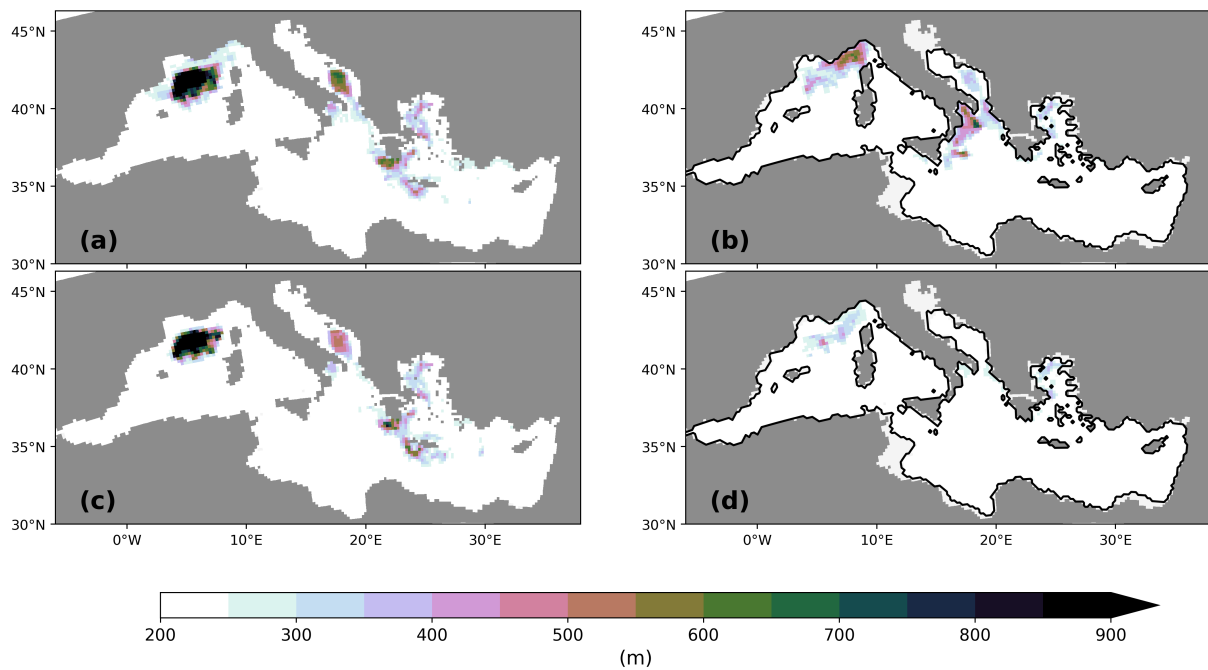
Figure A2. Maximum annual mixed layer depth (m) for the PI of GLAC1D (a) and for the LGM of GLAC-1D (b) and ICE-6G (d). Panel (c) give the information for PI-Straits. The contour line indicates the LGM coastline.
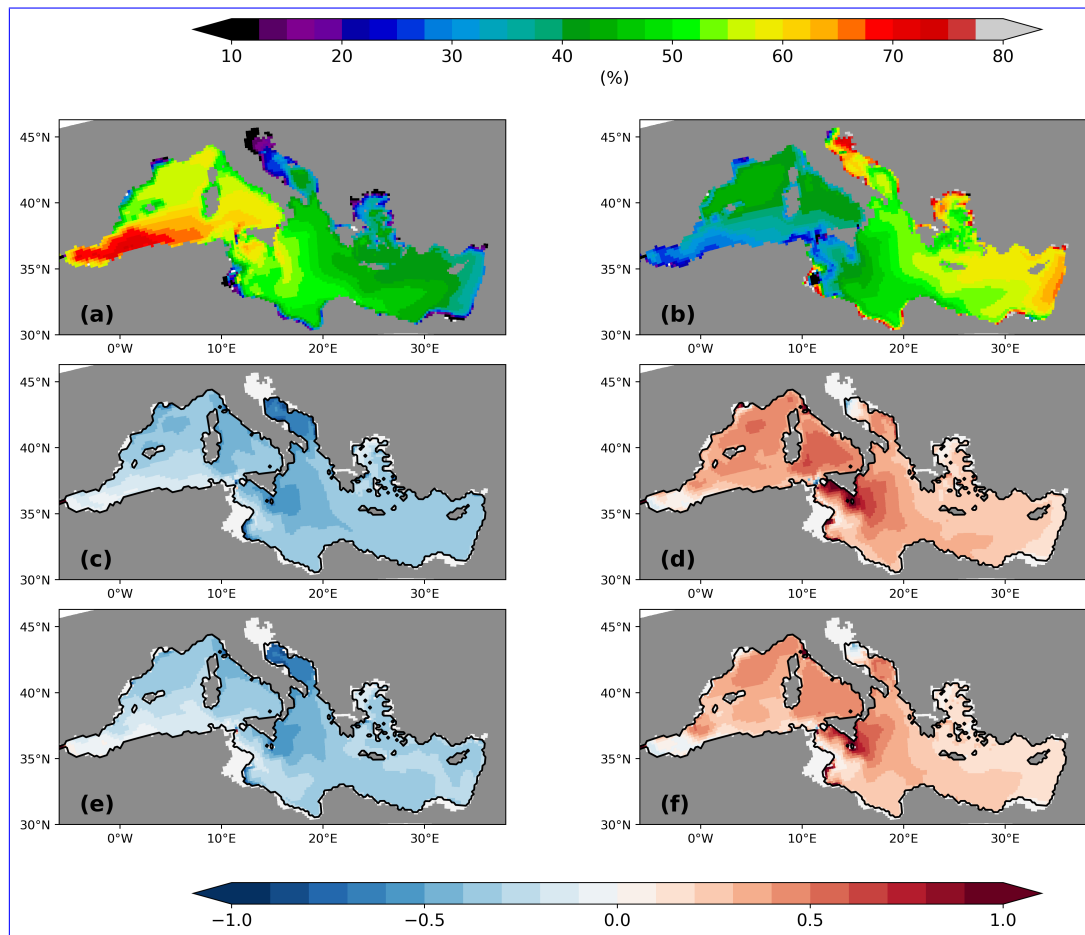
Figure A3. Weight-percentage sediment contribution in the upper 6 mm of the sediment column of calcite (a) and terrestrial material, i.e. clay, (b) for the PI of GLAC-1D (in %). Relative changes between LGM and the corresponding PI are given for calcite (c, e) and clay (d, f) for GLAC-1D (c, d) and ICE-6G (e, f).
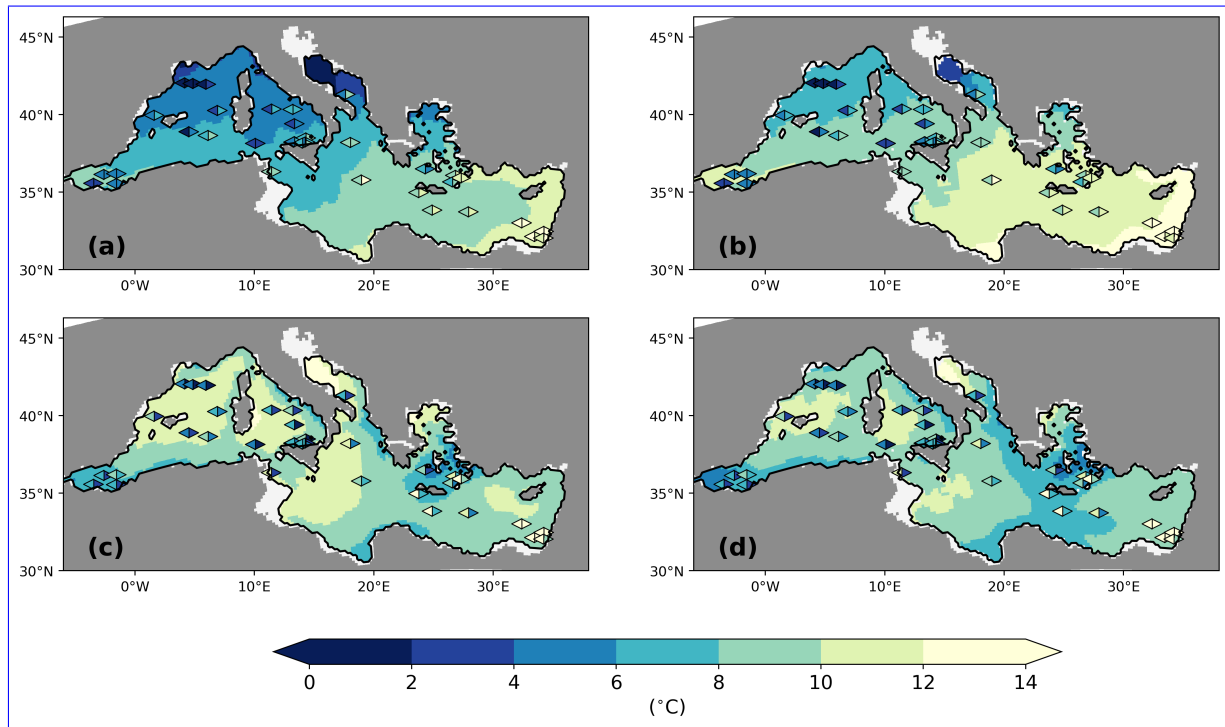
Figure A4. Annual minimum sea surface temperature (SST, a, b) and seasonal amplitude of SST (c, d) at the LGM for GLAC-1D (a,c) and ICE-6G (cbd). Seasonal amplitude is calculated from annual maximum and annual minimum. All units are in °C. Overlaid data from Hayes et al. (2005) for the same quantities estimated with two different methods: artificial neural network(left part of rhombu s) and the revised analogue method (right part of rhombus). See Hayes et al. (2005) for more details.
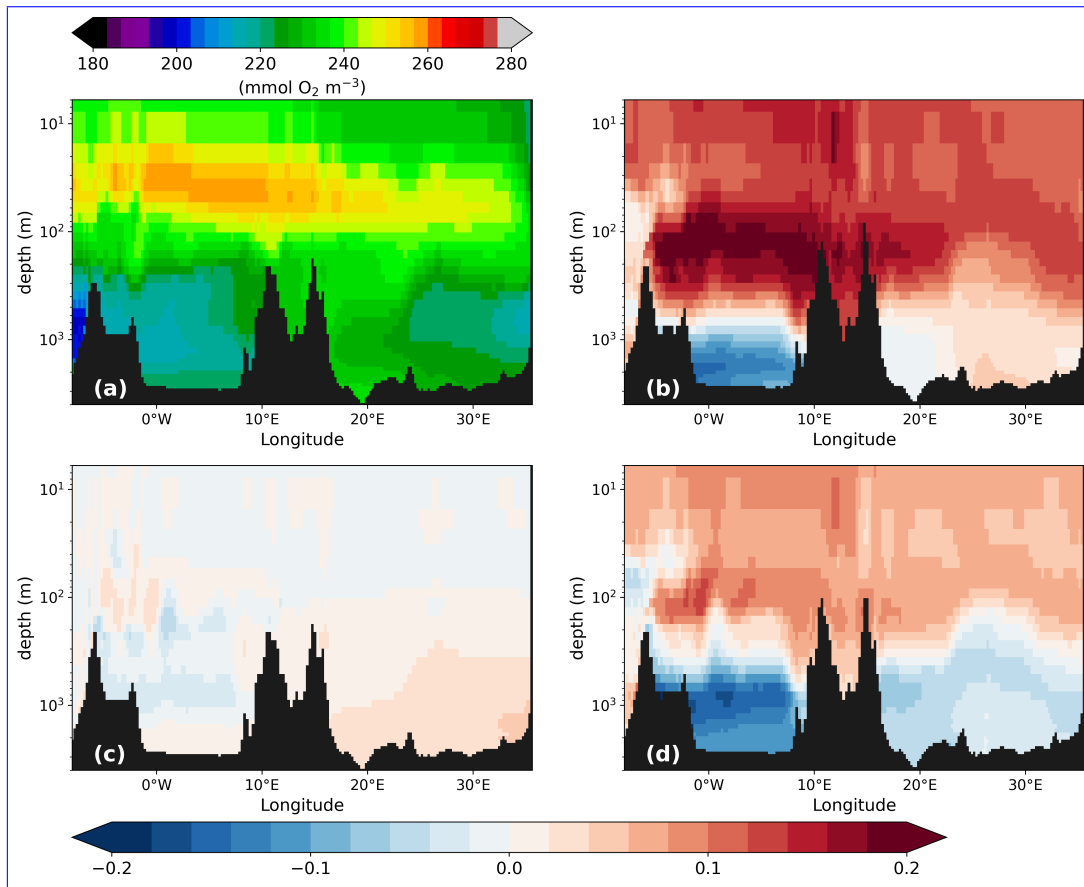
Figure A5. ~~Depth profiles~~ Similar to Fig. 13, but for ~~the Strait of Sicily of the~~ oxygen concentration ~~of dissolved (a) and organically bound phosphate (b), both in~~ mmol O_2 m^{-3}~~,)~~ along the ~~meridional transport through~~ east-west transect (for location see Fig. 1) of the ~~strait~~ PI of GLAC-1D (~~c, velocity times straits width, in 1000 m^2 s^{-1}~~a) ~~,~~ and the ~~transport for~~ relative concentration change between the ~~individual phosphate contributions which are combined shown in Fig. 15, as there is transport~~ LGM and the corresponding PI of ~~dissolved phosphate~~ GLAC-1D (b) and ICE-6G (d), and ~~transport of~~ between PI-Straits and the PI of ~~organically bound phosphate~~ GLAC-1D (~~e~~c)~~, both in mol m^{-1} s^{-1}~~. ~~Color coding as Fig~~Note the logarithmic depth scale in all panels. ~~15: GLAC-1D-PI~~Colder temperatures at the LGM increase the oxygen concentration in surface waters (~~black solid line~~)~~b,GLAC-1D-LGM (black dashed line~~d). The larger export of organic matter leads to oxygen consumption at depth, ~~and PI-Straits~~ but both deep basins are still well ventilated. The almost identical climate in PI-Strait (~~green line~~c) is reflected in a nearly identical oxygen concentration as in the PI. The small increase of O_2 concentrations in the eastern basin is attributable to a reduced organic matter flux to greater depth.
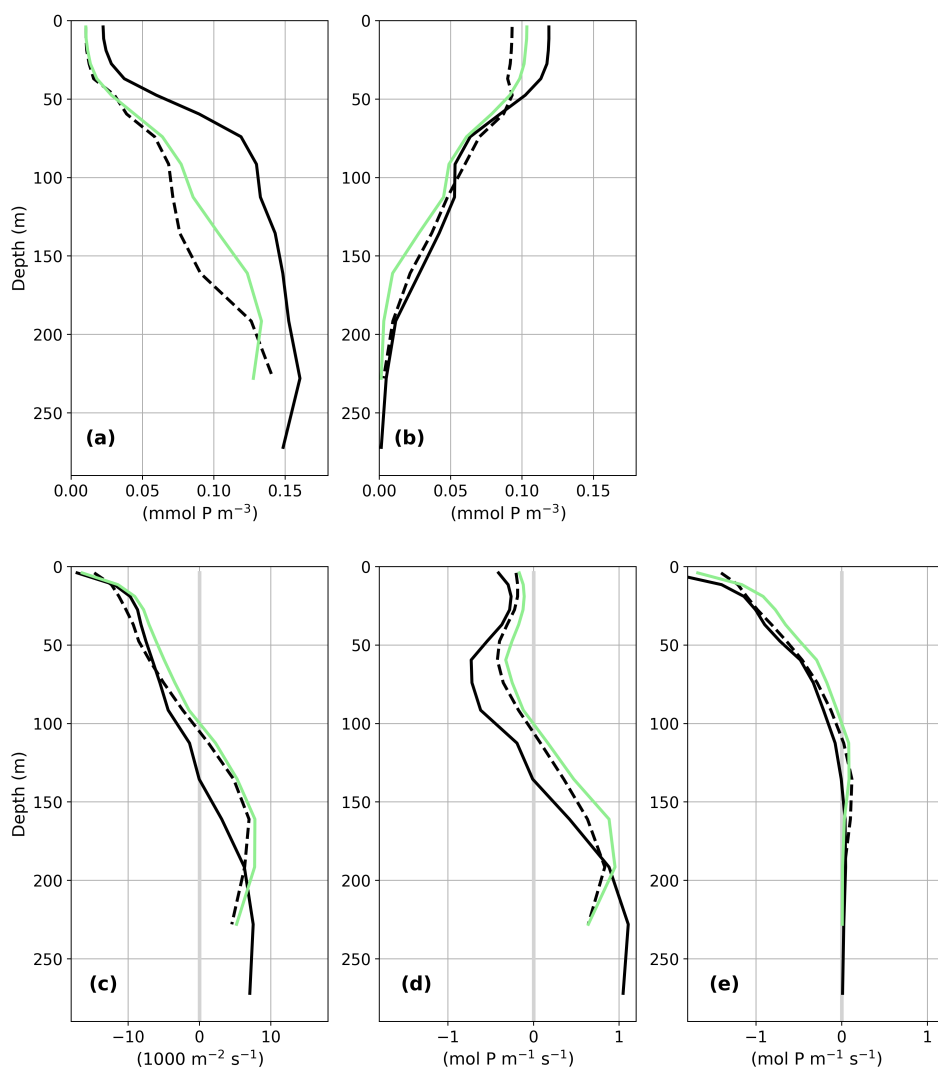
Figure A6. Depth profiles for the Strait of Sicily of the concentration of dissolved (a) and organically bound phosphate (b), both in mmol P m^{-3}, the meridional transport through the strait (c, velocity times straits width, in 1000 m^2 s^{-1}), and the transport for the individual phosphate contributions which are combined shown in Fig. 15, as there is transport of dissolved phosphate (d), and transport of of organically bound phosphate (e), both in mol P m^{-1} s^{-1}. Color coding as Fig. 15: GLAC-1D-PI (black solid line), GLAC-1D-LGM (black dashed line), and PI-Straits (green line).
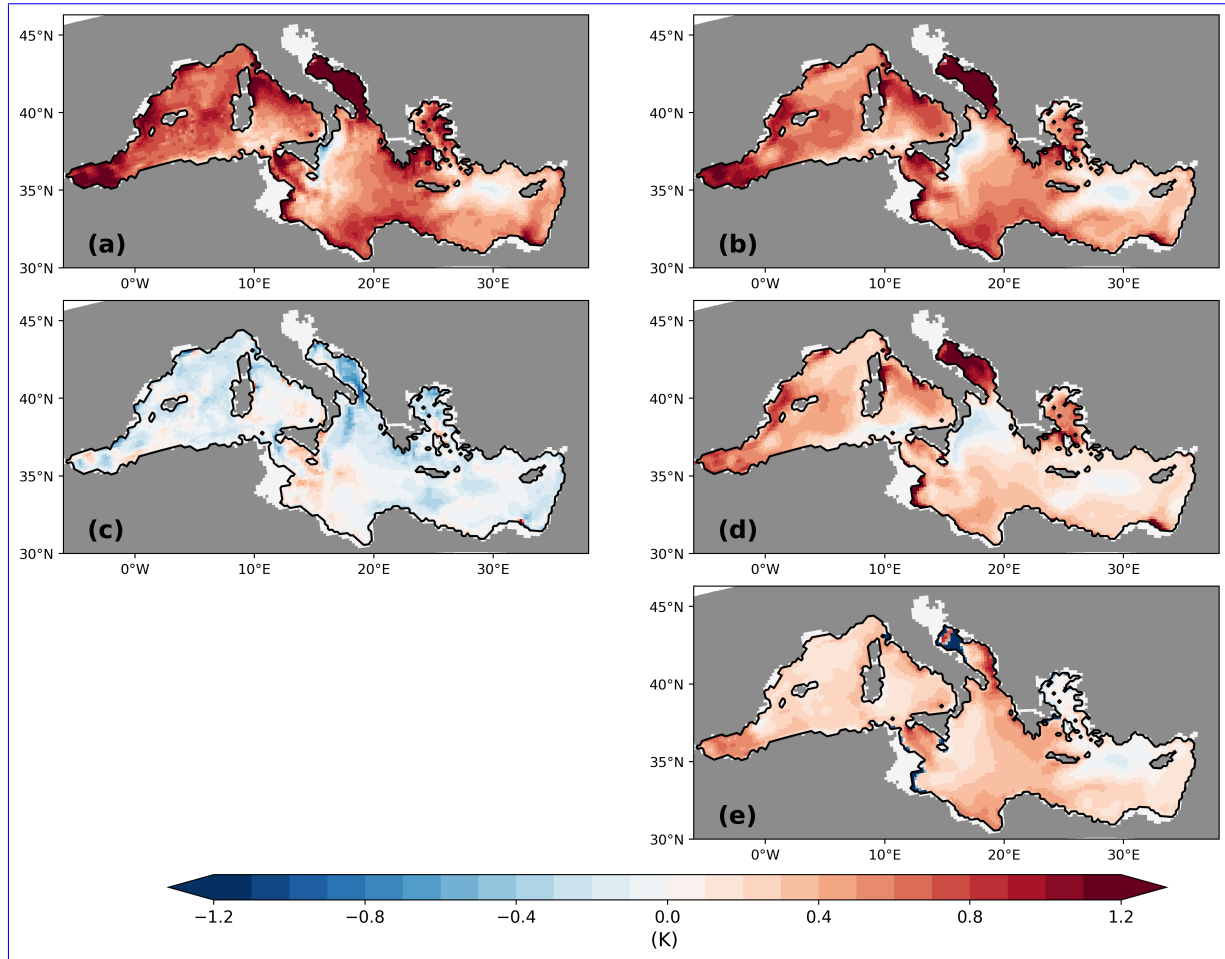
Figure A7. Same as Fig. 16, but for ICE-6G. Shown are the difference of ΔT_{org} and ΔT_{32} (a), the difference of ΔPWT and ΔT_{32} (b) and the difference between ΔPWT and ΔT_{org} (c). Panel (d) shows ΔPWT_{NPP}, the NPP related contribution to ΔPWT, and panel (e) displays ΔPWT_T - ΔT_{32}, the temperature related contribution. As for GLAC-1D, ΔT_{org} does not capture the full cooling signal given by ΔT_{32}.

Author contributions. U.M. and K.D.S. designed the experimental setups. K.D.S. performed and analysed all simulations. All authors critically discussed the presented results and contributed by providing valuable feedback during the manuscript compilation.

Competing interests. The authors declare that they have no conflict of interest.

Acknowledgements. ~~All simulations were performed at the German Climate Computing Center~~ We thank two anonymous reviewers for their constructive comments improving the earlier version of this paper. We also thank Anne Mouchet for her conscientious review which helped to fine-tune the first version of the manuscript. This work used resources of the Deutsches Klimarechenzentrum (DKRZ) granted by its Scientific Steering Committee (WLA) under project ID mh1212. Katharina D. Six is funded by the Deutsche Forschungsgemeinschaft (DFG, German Research Foundation) under Germany's Excellence Strategy – EXC 2037 'CLICCS - Climate, Climatic Change, and Society' – Project Number: 390683824.

References

Abu-Zied, R. H., Rohling, E. J., Jorissen, F. J., Fontanier, C., Casford, J. S., and Cooke, S.: Benthic foraminiferal response to changes in bottom-water oxygenation and organic carbon flux in the eastern Mediterranean during LGM to Recent times, Marine Micropaleontology, 67, 46–68, https://doi.org/10.1016/j.marmicro.2007.08.006, 2008.

555 Adloff, F., Mikolajewicz, U., Kučera, M., Grimm, R., Maier-Reimer, E., Schmiedl, G., and Emeis, K.-C.: Upper ocean climate of the Eastern Mediterranean Sea during the Holocene Insolation Maximum – a model study, Climate of the Past, 7, 1103–1122, https://doi.org/10.5194/cp-7-1103-2011, 2011.

Aksu, A., Yaşar, D., and Mudie, P.: Origin of late glacial—Holocene hemipelagic sediments in the Aegean Sea: clay mineralogy and carbonate cementation, Marine Geology, 123, 33–59, https://doi.org/10.1016/0025-3227(95)80003-t, 1995.

560 Albani, S., Mahowald, N. M., Murphy, L. N., Raiswell, R., Moore, J. K., Anderson, R. F., McGee, D., Bradtmiller, L. I., Delmonte, B., Hesse, P. P., and Mayewski, P. A.: Paleodust variability since the Last Glacial Maximum and implications for iron inputs to the ocean, Geophysical Research Letters, 43, 3944–3954, https://doi.org/10.1002/2016gl067911, 2016.

Allen, J. R. M., Brandt, U., Brauer, A., Hubberten, H.-W., Huntley, B., Keller, J., Kraml, M., Mackensen, A., Mingram, J., Negendank, J. F. W., Nowaczyk, N. R., Oberhänsli, H., Watts, W. A., Wulf, S., and Zolitschka, B.: Rapid environmental changes in southern Europe
565 during the last glacial period, Nature, 400, 740–743, https://doi.org/10.1038/23432, 1999.

Ausín, B., Flores, J.-A., Sierro, F.-J., Bárcena, M.-A., Hernández-Almeida, I., Francés, G., Gutiérrez-Arnillas, E., Martrat, B., Grimalt, J., and Cacho, I.: Coccolithophore productivity and surface water dynamics in the Alboran Sea during the last 25 kyr, Palaeogeography, Palaeoclimatology, Palaeoecology, 418, 126–140, https://doi.org/10.1016/j.palaeo.2014.11.011, 2015.

Béjard, T. M., Rigual-Hernández, A. S., Flores, J. A., Tarruella, J. P., de Madron, X. D., Cacho, I., Haghipour, N., Hunter, A., and Sierro,
570 F. J.: Calcification response of planktic foraminifera to environmental change in the western Mediterranean Sea during the industrial era, Biogeosciences, 20, 1505–1528, https://doi.org/10.5194/bg-20-1505-2023, 2023.

Belgacem, M., Schroeder, K., Barth, A., Troupin, C., Pavoni, B., Raimbault, P., Garcia, N., Borghini, M., and Chiggiato, J.: Climatological distribution of dissolved inorganic nutrients in the western Mediterranean Sea (1981–2017), Earth System Science Data, 13, 5915–5949, https://doi.org/10.5194/essd-13-5915-2021, 2021.

575 Betzer, P. R., Showers, W. J., Laws, E. A., Winn, C. D., DiTullio, G. R., and Kroopnick, P. M.: Primary productivity and particle fluxes on a transect of the equator at 153°W in the Pacific Ocean, Deep Sea Research Part A. Oceanographic Research Papers, 31, 1–11, https://doi.org/10.1016/0198-0149(84)90068-2, 1984.

Bidle, K. D., Manganelli, M., and Azam, F.: Regulation of Oceanic Silicon and Carbon Preservation by Temperature Control on Bacteria, Science, 298, 1980–1984, https://doi.org/10.1126/science.1076076, 2002.

580 Bopp, L., Kohfeld, K. E., Quéré, C. L., and Aumont, O.: Dust impact on marine biota and atmospheric CO_2 during glacial periods, Paleoceanography, 18, https://doi.org/10.1029/2002pa000810, 2003.

Bosc, E., Bricaud, A., and Antoine, D.: Seasonal and interannual variability in algal biomass and primary production in the Mediterranean Sea, as derived from 4 years of SeaWiFS observations, Global Biogeochemical Cycles, 18, https://doi.org/10.1029/2003gb002034, 2004.

Box, M., Krom, M., Cliff, R., Bar-Matthews, M., Almogi-Labin, A., Ayalon, A., and Paterne, M.: Response of the Nile and its catchment
585 to millennial-scale climatic change since the LGM from Sr isotopes and major elements of East Mediterranean sediments, Quaternary Science Reviews, 30, 431–442, https://doi.org/10.1016/j.quascirev.2010.12.005, 2011.

Candela, J.: Chapter 5.7 Mediterranean water and global circulation, p. 419–XLVIII, Elsevier, https://doi.org/10.1016/s0074-6142(01)80132-7, 2001.

Castañeda, I. S., Schefuß, E., Pätzold, J., Sinninghe Damsté, J. S., Weldeab, S., and Schouten, S.: Isoprenoidal GDGT and alkenone-based

590   proxies of sediment core GeoB7702-3, https://doi.org/10.1594/PANGAEA.736909, 2010.

Colin, C., Duhamel, M., Siani, G., Dubois-Dauphin, Q., Ducassou, E., Liu, Z., Wu, J., Revel, M., Dapoigny, A., Douville, E., Taviani, M., and Montagna, P.: Changes in the Intermediate Water Masses of the Mediterranean Sea During the Last Climatic Cycle—New Constraints From Neodymium Isotopes in Foraminifera, Paleoceanography and Paleoclimatology, 36, https://doi.org/10.1029/2020pa004153, 2021.

Conte, M. H., Sicre, M.-A., Rühlemann, C., Weber, J. C., Schulte, S., Schulz-Bull, D., and Blanz, T.: Global temperature calibration of the

595   alkenone unsaturation index ($U_{37}^{K'}$) in surface waters and comparison with surface sediments, Geochemistry, Geophysics, Geosystems, 7, https://doi.org/10.1029/2005gc001054, 2006.

Cornuault, M., Tachikawa, K., Vidal, L., Guihou, A., Siani, G., Deschamps, P., Bassinot, F., and Revel, M.: Circulation Changes in the Eastern Mediterranean Sea Over the Past 23, 000 Years Inferred From Authigenic Nd Isotopic Ratios, Paleoceanography and Paleoclimatology, 33, 264–280, https://doi.org/10.1002/2017pa003227, 2018.

600 Dubois, C., Somot, S., Calmanti, S., Carillo, A., Déqué, M., Dell'Aquila, A., Elizalde, A., Gualdi, S., Jacob, D., L'Hévéder, B., Li, L., Oddo, P., Sannino, G., Scoccimarro, E., and Sevault, F.: Future projections of the surface heat and water budgets of the Mediterranean Sea in an ensemble of coupled atmosphere–ocean regional climate models, Climate Dynamics, 39, 1859–1884, https://doi.org/10.1007/s00382-011-1261-4, 2011.

Duhamel, M., Colin, C., Revel, M., Siani, G., Dapoigny, A., Douville, E., Wu, J., Zhao, Y., Liu, Z., and Montagna, P.: Variations in eastern

605   Mediterranean hydrology during the last climatic cycle as inferred from neodymium isotopes in foraminifera, Quaternary Science Reviews, 237, 106 306, https://doi.org/10.1016/j.quascirev.2020.106306, 2020.

D'Ortenzio, F. and Ribera d'Alcalà, M.: On the trophic regimes of the Mediterranean Sea: a satellite analysis, Biogeosciences, 6, 139–148, https://doi.org/10.5194/bg-6-139-2009, 2009.

Emeis, K.-C., Struck, U., Schulz, H.-M., Rosenberg, R., Bernasconi, S., Erlenkeuser, H., Sakamoto, T., and Martinez-Ruiz, F.: Temperature

610   and salinity variations of Mediterranean Sea surface waters over the last 16, 000 years from records of planktonic stable oxygen isotopes and alkenone unsaturation ratios, Palaeogeography, Palaeoclimatology, Palaeoecology, 158, 259–280, https://doi.org/10.1016/s0031-0182(00)00053-5, 2000.

Garcia, H., Weathers, K., Paver, C., Smolyar, I., Boyer, T., Locarnini, R., Zweng, M., Mishonov, A., Baranova, O., Seidov, D., and Reagan, J.: World Ocean Atlas 2018, Vol. 4: Dissolved Inorganic Nutrients (phosphate, nitrate and nitrate+nitrite, silicat), Tech. rep., A. Mishonov

615   Technical Ed.; NOAA Atlas NESDIS 84, 35 pp., 2019a.

Garcia, H., Weathers, K., Paver, C., Smolyar, I., Boyer, T., Locarnini, R., Zweng, M., Mishonov, A., Baranova, O., Seidov, D., and Reagan, J.: World Ocean Atlas 2018, Volume 3: Dissolved Oxygen, Apparent Oxygen Utilization, and Oxygen Saturation, Tech. rep., A. Mishonov Technical Ed.; NOAA Atlas NESDIS 83, 38 pp., 2019b.

Gent, P., Willebrand, J., McDougall, T., and McWilliams, J.: Parameterizing Eddy-Induced Tracer Transports in Ocean Circulation Models,

620   Journal of Physical Oceanography, 25, 463–474, https://doi.org/10.1175/1520-0485(1995)025<0463:PEITTI>2.0.CO;2, 1995.

Goldsmith, Y., Polissar, P., Ayalon, A., Bar-Matthews, M., deMenocal, P., and Broecker, W.: The modern and Last Glacial Maximum hydrological cycles of the Eastern Mediterranean and the Levant from a water isotope perspective, Earth and Planetary Science Letters, 457, 302–312, https://doi.org/10.1016/j.epsl.2016.10.017, 2017.

Grimm, R., Maier-Reimer, E., Mikolajewicz, U., Schmiedl, G., Müller-Navarra, K., Adloff, F., Grant, K. M., Ziegler, M., Lourens, L. J., and Emeis, K.-C.: Late glacial initiation of Holocene eastern Mediterranean sapropel formation, Nature Communications, 6, https://doi.org/10.1038/ncomms8099, 2015.

Hamann, Y., Ehrmann, W., Schmiedl, G., Krüger, S., Stuut, J.-B., and Kuhnt, T.: Sedimentation processes in the Eastern Mediterranean Sea during the Late Glacial and Holocene revealed by end-member modelling of the terrigenous fraction in marine sediments, Marine Geology, 248, 97–114, https://doi.org/10.1016/j.margeo.2007.10.009, 2008.

Hayes, A., Kucera, M., Kallel, N., Sbaffi, L., and Rohling, E. J.: Glacial Mediterranean sea surface temperatures based on planktonic foraminiferal assemblages, Quaternary Science Reviews, 24, 999–1016, https://doi.org/10.1016/j.quascirev.2004.02.018, 2005.

Heinze, C., Maier-Reimer, E., Winguth, A. M. E., and Archer, D.: A global oceanic sediment model for long-term climate studies, Global Biogeochemical Cycles, 13, 221–250, https://doi.org/10.1029/98GB02812, 1999.

Herbert, T. D., Lawrence, K. T., Tzanova, A., Peterson, L. C., Caballero-Gill, R. P., and Kelly, C. S.: (Table S2) SST esimates as a function of age, Mediterranean sites, https://doi.org/10.1594/PANGAEA.885603, 2018.

Hoogakker, B., Rothwell, R., Rohling, E., Paterne, M., Stow, D., Herrle, J., and Clayton, T.: Variations in terrigenous dilution in western Mediterranean Sea pelagic sediments in response to climate change during the last glacial cycle, Marine Geology, 211, 21–43, https://doi.org/10.1016/j.margeo.2004.07.005, 2004.

Ilyina, T., Six, K., Segschneider, J., Maier-Reimer, E., Li, H., and Núñez-Riboni, I.: Global ocean biogeochemistry model HAMOCC: Model architecture and performance as component of the MPI-Earth System Model in different CMIP5 experimental realizations, Journal of Advances in Modeling Earth Systems, https://doi.org/10.1029/2012MS000178, 2013.

Johnson, K. S., Gordon, R. M., and Coale, K. H.: What controls dissolved iron concentrations in the world ocean?, Marine Chemistry, 57, 137–161, https://doi.org/10.1016/s0304-4203(97)00043-1, 1997.

Jungclaus, J. H., Fischer, N., Haak, H., Lohmann, K., Marotzke, J., Matei, D., Mikolajewicz, U., Notz, D., and Storch, J. S.: Characteristics of the ocean simulations in the Max Planck Institute Ocean Model (MPIOM) the ocean component of the MPI-Earth system model, Journal of Advances in Modeling Earth Systems, 5, 422–446, https://doi.org/10.1002/jame.20023, 2013.

Kageyama, M., Harrison, S. P., Kapsch, M.-L., Lofverstrom, M., Lora, J. M., Mikolajewicz, U., Sherriff-Tadano, S., Vadsaria, T., Abe-Ouchi, A., Bouttes, N., Chandan, D., Gregoire, L. J., Ivanovic, R. F., Izumi, K., LeGrande, A. N., Lhardy, F., Lohmann, G., Morozova, P. A., Ohgaito, R., Paul, A., Peltier, W. R., Poulsen, C. J., Quiquet, A., Roche, D. M., Shi, X., Tierney, J. E., Valdes, P. J., Volodin, E., and Zhu, J.: The PMIP4 Last Glacial Maximum experiments: preliminary results and comparison with the PMIP3 simulations, Climate of the Past, 17, 1065–1089, https://doi.org/10.5194/cp-17-1065-2021, 2021.

Kapsch, M.-L., Mikolajewicz, U., Ziemen, F., and Schannwell, C.: Ocean Response in Transient Simulations of the Last Deglaciation Dominated by Underlying Ice-Sheet Reconstruction and Method of Meltwater Distribution, Geophysical Research Letters, 49, e2021GL096 767, https://doi.org/https://doi.org/10.1029/2021GL096767, 2022.

Kohfeld, K. E., Quéré, C. L., Harrison, S. P., and Anderson, R. F.: Role of Marine Biology in Glacial-Interglacial CO_2 Cycles, Science, 308, 74–78, https://doi.org/10.1126/science.1105375, 2005.

Kotthoff, U., Müller, U. C., Pross, J., Schmiedl, G., Lawson, I. T., van de Schootbrugge, B., and Schulz, H.: Lateglacial and Holocene vegetation dynamics in the Aegean region: an integrated view based on pollen data from marine and terrestrial archives, The Holocene, 18, 1019–1032, https://doi.org/10.1177/0959683608095573, 2008.

660 Koutsodendris, A., Dakos, V., Fletcher, W. J., Knipping, M., Kotthoff, U., Milner, A. M., Müller, U. C., Kaboth-Bahr, S., Kern, O. A., Kolb, L., Vakhrameeva, P., Wulf, S., Christanis, K., Schmiedl, G., and Pross, J.: Atmospheric CO2 forcing on Mediterranean biomes during the past 500 kyrs, Nature Communications, 14, https://doi.org/10.1038/s41467-023-37388-x, 2023.

Kriest, I. and Oschlies, A.: On the treatment of particulate organic matter sinking in large-scale models of marine biogeochemical cycles, Biogeosciences, 5, 55–72, https://doi.org/10.5194/bg-5-55-2008, 2008.

665 Krom, M., Kress, N., Berman-Frank, I., and Rahav, E.: Past, Present and Future Patterns in the Nutrient Chemistry of the Eastern Mediterranean, in: The Mediterranean Sea, edited by Goffredo, S. and Dubinsky, Z., pp. 49–68, Springer Netherlands, https://doi.org/10.1007/978-94-007-6704-1, 2014.

Kuhlemann, J., Rohling, E. J., Krumrei, I., Kubik, P., Ivy-Ochs, S., and Kucera, M.: Regional Synthesis of Mediterranean Atmospheric Circulation During the Last Glacial Maximum, Science, 321, 1338–1340, https://doi.org/10.1126/science.1157638, 2008.

670 Kuhnt, T., Schmiedl, G., Ehrmann, W., Hamann, Y., and Hemleben, C.: Deep-sea ecosystem variability of the Aegean Sea during the past 22 kyr as revealed by Benthic Foraminifera, Marine Micropaleontology, 64, 141–162, https://doi.org/10.1016/j.marmicro.2007.04.003, 2007.

Lacombe, H. and Richez, C.: The Regime of the Strait of Gibraltar, in: Hydrodynamics of Semi-Enclosed Seas, Proceedings of the 13th International Liege Colloquium on Ocean Hydrodynamics, pp. 13–73, Elsevier, https://doi.org/10.1016/s0422-9894(08)71237-6, 1982.

675 Lambeck, K., Rouby, H., Purcell, A., Sun, Y., and Sambridge, M.: Sea level and global ice volumes from the Last Glacial Maximum to the Holocene, Proceedings of the National Academy of Sciences, 111, 15 296–15 303, https://doi.org/10.1073/pnas.1411762111, 2014.

Laufkötter, C., John, J. G., Stock, C. A., and Dunne, J. P.: Temperature and oxygen dependence of the remineralization of organic matter, Global Biogeochemical Cycles, 31, 1038–1050, https://doi.org/10.1002/2017gb005643, 2017.

Lauvset, S. K., Lange, N., Tanhua, T., Bittig, H. C., Olsen, A., Kozyr, A., Álvarez, M., Becker, S., Brown, P. J., Carter, B. R., Cotrim da
680 Cunha, L., Feely, R. A., van Heuven, S., Hoppema, M., Ishii, M., Jeansson, E., Jutterström, S., Jones, S. D., Karlsen, M. K., Lo Monaco, C., Michaelis, P., Murata, A., Pérez, F. F., Pfeil, B., Schirnick, C., Steinfeldt, R., Suzuki, T., Tilbrook, B., Velo, A., Wanninkhof, R., Woosley, R. J., and Key, R. M.: An updated version of the global interior ocean biogeochemical data product, GLODAPv2.2021, Earth System Science Data, 13, 5565–5589, https://doi.org/10.5194/essd-13-5565-2021, 2021.

Lee, K. E.: Compilation of alkenone LGM SST data, https://doi.org/10.1594/PANGAEA.103070, 2004.

685 Liu, F., Mikolajewicz, U., and Six, K. D.: Drivers of the decadal variability of the North Ionian Gyre upper layer circulation during 1910–2010: a regional modelling study, Climate Dynamics, 58, 2065–2077, https://doi.org/10.1007/s00382-021-05714-y, 2021.

Locarnini, R. A., Mishonov, A. V., Baranova, O. K., Boyer, T. P., Zweng, M. M., Garcia, H. E., Reagan, J. R., Seidov, D., Weathers, K. W., Paver, C. R., and Smolyar, I. V.: World Ocean Atlas 2018, Volume 1: Temperature, Tech. rep., A. Mishonov Technical Ed.; NOAA Atlas NESDIS 81, 52 pp., 2018.

690 Löfverström, M.: A dynamic link between high-intensity precipitation events in southwestern North America and Europe at the Last Glacial Maximum, Earth and Planetary Science Letters, 534, 116 081, https://doi.org/10.1016/j.epsl.2020.116081, 2020.

Löfverström, M. and Lora, J. M.: Abrupt regime shifts in the North Atlantic atmospheric circulation over the last deglaciation, Geophysical Research Letters, 44, 8047–8055, https://doi.org/10.1002/2017gl074274, 2017.

Ludwig, W., Dumont, E., Meybeck, M., and Heussner, S.: River discharges of water and nutrients to the Mediterranean and
695 Black Sea: Major drivers for ecosystem changes during past and future decades?, Progress in Oceanography, 80, 199–217, https://doi.org/10.1016/j.pocean.2009.02.001, 2009.

Martin, J. H., Knauer, G. A., Karl, D. M., and Broenkow, W. W.: VERTEX: carbon cycling in the northeast Pacific, Deep Sea Research Part A. Oceanographic Research Papers, 34, 267–285, https://doi.org/10.1016/0198-0149(87)90086-0, 1987.

Mathis, M., Elizalde, A., and Mikolajewicz, U.: The future regime of Atlantic nutrient supply to the Northwest European Shelf, Journal of Marine Systems, 189, 98–115, https://doi.org/10.1016/j.jmarsys.2018.10.002, 2019.

Mauritsen, T., Bader, J., Becker, T., Behrens, J., Bittner, M., Brokopf, R., and et al.: Developments in the MPI-M Earth System Model version 1.2 (MPI-ESM1.2) and Its Response to Increasing CO2, Journal of Advances in Modeling Earth System, 11, 998–1038, https://doi.org/10.1029/ 2018MS001400, 2019.

Meccia, V. L. and Mikolajewicz, U.: Interactive ocean bathymetry and coastlines for simulating the last deglaciation with the Max Planck Institute Earth System Model (MPI-ESM-v1.2), Geoscientific Model Development, 11, 4677–4692, https://doi.org/10.5194/gmd-11-4677-2018, 2018.

MEDAR Group: MEDATLAS/2002 database. Mediterranean and Black Sea database of temperature salinity and bio-chemical parameters, Climatological Atlas. IFREMER Edition (4 Cdroms), 2002.

Menviel, L., Timmermann, A., Mouchet, A., and Timm, O.: Meridional reorganizations of marine and terrestrial productivity during Heinrich events, Paleoceanography, 23, https://doi.org/10.1029/2007pa001445, 2008.

Mikolajewicz, U.: Modeling Mediterranean Ocean climate of the Last Glacial Maximum, Climate of the Past, 7, 161–180, https://doi.org/10.5194/cp-7-161-2011, 2011.

Morée, A. L., Schwinger, J., Ninnemann, U. S., Jeltsch-Thömmes, A., Bethke, I., and Heinze, C.: Evaluating the biological pump efficiency of the Last Glacial Maximum ocean using $\delta^{13}C$, Climate of the Past, 17, 753–774, https://doi.org/10.5194/cp-17-753-2021, 2021.

Müller, P. J., Kirst, G., Ruhland, G., von Storch, I., and Rosell-Melé, A.: Calibration of the alkenone paleotemperature index $U_{37}^{K'}$ based on core-tops from the eastern South Atlantic and the global ocean (60°N-60°S), Geochimica et Cosmochimica Acta, 62, 1757–1772, https://doi.org/10.1016/s0016-7037(98)00097-0, 1998.

Myers, P. G., Haines, K., and Rohling, E. J.: Modeling the paleocirculation of the Mediterranean: The Last Glacial Maximum and the Holocene with emphasis on the formation of sapropel S_1, Paleoceanography, 13, 586–606, https://doi.org/10.1029/98pa02736, 1998.

Pacanowski, R. C. and Philander, S. G. H.: Parameterization of Vertical Mixing in Numerical Models of Tropical Oceans, Journal of Physical Oceanography, 11, 1443–1451, https://doi.org/10.1175/1520-0485(1981)011<1443:povmin>2.0.co;2, 1981.

Palastanga, V., Slomp, C. P., and Heinze, C.: Glacial-interglacial variability in ocean oxygen and phosphorus in a global biogeochemical model, Biogeosciences, 10, 945–958, https://doi.org/10.5194/bg-10-945-2013, 2013.

Paulsen, H., Ilyina, T., Six, K. D., and Stemmler, I.: Incorporating a prognostic representation of marine nitrogen fixers into the global ocean biogeochemical model HAMOCC, Journal of Advances in Modeling Earth Systems, 9, 438–464, https://doi.org/10.1002/2016ms000737, 2017.

Pedrosa-Pàmies, R., Parinos, C., Sanchez-Vidal, A., Gogou, A., Calafat, A., Canals, M., Bouloubassi, I., and Lampadariou, N.: Composition and sources of sedimentary organic matter in the deep eastern Mediterranean Sea, Biogeosciences, 12, 7379–7402, https://doi.org/10.5194/bg-12-7379-2015, 2015.

Peltier, W. R., Argus, D. F., and Drummond, R.: Space geodesy constrains ice age terminal deglaciation: The global ICE-6G_C (VM5a) model, Journal of Geophysical Research: Solid Earth, 120, 450–487, https://doi.org/10.1002/2014jb011176, 2015.

Pinardi, N., Cessi, P., Borile, F., and Wolfe, C. L. P.: The Mediterranean Sea Overturning Circulation, Journal of Physical Oceanography, 49, 1699–1721, https://doi.org/10.1175/jpo-d-18-0254.1, 2019.

Poli, P., Hersbach, H., Dee, D. P., Berrisford, P., Simmons, A. J., Vitart, F., Laloyaux, P., Tan, D. G. H., Peubey, C., Thépaut, J.-N., Trémolet, Y., Hólm, E. V., Bonavita, M., Isaksen, L., and Fisher, M.: ERA-20C: An Atmospheric Reanalysis of the Twentieth Century, Journal of Climate, 29, 4083 – 4097, https://doi.org/10.1175/JCLI-D-15-0556.1, 2016.

Radi, T. and de Vernal, A.: Last glacial maximum (LGM) primary productivity in the northern North Atlantic Ocean, Canadian Journal of Earth Sciences, 45, 1299–1316, https://doi.org/10.1139/e08-059, 2008.

Reale, M., Giorgi, F., Solidoro, C., Di Biagio, V., Di Sante, F., Mariotti, L., Farneti, R., and Sannino, G.: The Regional Earth System Model RegCM-ES: Evaluation of the Mediterranean Climate and Marine Biogeochemistry, Journal of Advances in Modeling Earth Systems, 12, https://doi.org/10.1029/2019ms001812, 2020.

Reale, M., Cossarini, G., Lazzari, P., Lovato, T., Bolzon, G., Masina, S., Solidoro, C., and Salon, S.: Acidification, deoxygenation, and nutrient and biomass declines in a warming Mediterranean Sea, Biogeosciences, 19, 4035–4065, https://doi.org/10.5194/bg-19-4035-2022, 2022.

Redi, M. H.: Oceanic Isopycnal Mixing by Coordinate Rotation, Journal of Physical Oceanography, 12, 1154–1158, https://doi.org/10.1175/1520-0485(1982)012<1154:oimbcr>2.0.co;2, 1982.

Revel, M., Colin, C., Bernasconi, S., Combourieu-Nebout, N., Ducassou, E., Grousset, F. E., Rolland, Y., Migeon, S., Bosch, D., Brunet, P., Zhao, Y., and Mascle, J.: 21, 000 Years of Ethiopian African monsoon variability recorded in sediments of the western Nile deep-sea fan, Regional Environmental Change, 14, 1685–1696, https://doi.org/10.1007/s10113-014-0588-x, 2014.

Riddick, T., Brovkin, V., Hagemann, S., and Mikolajewicz, U.: Dynamic hydrological discharge modelling for coupled climate model simulations of the last glacial cycle: the MPI-DynamicHD model version 3.0, Geoscientific Model Development, 11, 4291–4316, https://doi.org/10.5194/gmd-11-4291-2018, 2018.

Rijk, S. D., Jorissen, F., Rohling, E., and Troelstra, S.: Organic flux control on bathymetric zonation of Mediterranean benthic foraminifera, Marine Micropaleontology, 40, 151–166, https://doi.org/10.1016/s0377-8398(00)00037-2, 2000.

Rodrigo-Gámiz, M., Martinez-Ruiz, F. C., Rampen, S. W., Schouten, S., and Sinninghe Damsté, J. S.: Sea surface temperature reconstruction of sediment core TTR12_293G, https://doi.org/10.1594/PANGAEA.826065, 2014.

Rohling, E., Marino, G., and Grant, K.: Mediterranean climate and oceanography, and the periodic development of anoxic events (sapropels), Earth-Science Reviews, 143, 62–97, https://doi.org/10.1016/j.earscirev.2015.01.008, 2015.

Rohling, E. J.: A Simple Two-Layered Model for Shoaling of the Eastern Mediterranean Pycnocline Due to Glacio-Eustatic Sea Level Lowering, Paleoceanography, 6, 537–541, https://doi.org/10.1029/91pa01328, 1991.

Rohling, E. J. and Gieskes, W. W. C.: Late Quaternary changes in Mediterranean intermediate water density and formation rate, Paleoceanography, 4, 531–545, https://doi.org/10.1029/pa004i005p00531, 1989.

Rosell-Melé, A. and Prahl, F. G.: Seasonality of $U^{K'}_{37}$ temperature estimates as inferred from sediment trap data, Quaternary Science Reviews, 72, 128–136, https://doi.org/10.1016/j.quascirev.2013.04.017, 2013.

Sanchez-Gomez, E., Somot, S., Josey, S. A., Dubois, C., Elguindi, N., and Déqué, M.: Evaluation of Mediterranean Sea water and heat budgets simulated by an ensemble of high resolution regional climate models, Climate Dynamics, 37, 2067–2086, https://doi.org/10.1007/s00382-011-1012-6, 2011.

Schmiedl, G., Hemleben, C., Keller, J., and Segl, M.: Impact of climatic changes on the benthic foraminiferal fauna in the Ionian Sea during the last 330, 0000 years, Paleoceanography, 13, 447–458, https://doi.org/10.1029/98pa01864, 1998.

Schmiedl, G., Kuhnt, T., Ehrmann, W., Emeis, K.-C., Hamann, Y., Kotthoff, U., Dulski, P., and Pross, J.: Climatic forcing of eastern Mediterranean deep-water formation and benthic ecosystems during the past 22 000 years, Quaternary Science Reviews, 29, 3006–3020, https://doi.org/10.1016/j.quascirev.2010.07.002, 2010.

Schmiedl, G., Milker, Y., and Mackensen, A.: Climate forcing of regional deep-sea biodiversity documented by benthic foraminifera, Earth-Science Reviews, 244, 104 540, https://doi.org/10.1016/j.earscirev.2023.104540, 2023.

Schrag, D. P., Adkins, J. F., McIntyre, K., Alexander, J. L., Hodell, D. A., Charles, C. D., and McManus, J. F.: The oxygen isotopic composition of seawater during the Last Glacial Maximum, Quaternary Science Reviews, 21, 331–342, https://doi.org/10.1016/s0277-3791(01)00110-x, 2002.

Sevault, F., Somot, S., Alias, A., Dubois, C., Lebeaupin-Brossier, C., Nabat, P., Adloff, F., Déqué, M., and Decharme, B.: A fully coupled Mediterranean regional climate system model: design and evaluation of the ocean component for the 1980–2012 period, Tellus A: Dynamic Meteorology and Oceanography, 66, 23 967, https://doi.org/10.3402/tellusa.v66.23967, 2014.

Sijinkumar, A., Clemens, S., Nath, B. N., Prell, W., Benshila, R., and Lengaigne, M.: δ^{18}O and salinity variability from the Last Glacial Maximum to Recent in the Bay of Bengal and Andaman Sea, Quaternary Science Reviews, 135, 79–91, https://doi.org/10.1016/j.quascirev.2016.01.022, 2016.

Six, K. D.: Model data of the physical-biogeochemical state of the Mediterranean Sea during the Last Glacial Maximum [Data set], https://doi.org/10.5281/zenodo.10624618, 2024.

Six, K. D., , and Maier-Reimer, E.: Effects of plankton dynamics on seasonal carbon fluxes in an ocean general circulation model, Global Biogeochem. Cycles, p. 559–583, 1996.

Steele, M., Morley, R., and Ermold, W.: PHC: A Global Ocean Hydrography with a High-Quality Arctic Ocean, Journal of Climate, 14, 2079–2087, https://doi.org/10.1175/1520-0442(2001)014<2079:pagohw>2.0.co;2, 2001.

Takahashi, T., Broecker, W., and Langer, S.: Redfield ratio based on chemical data from isopycnal surfaces, J. Geophys. Res., p. 6907–6924, 1985.

Tamburini, F. and Föllmi, K. B.: Phosphorus burial in the ocean over glacial-interglacial time scales, Biogeosciences, 6, 501–513, https://doi.org/10.5194/bg-6-501-2009, 2009.

Tarasov, L., Dyke, A. S., Neal, R. M., and Peltier, W.: A data-calibrated distribution of deglacial chronologies for the North American ice complex from glaciological modeling, Earth and Planetary Science Letters, 315-316, 30–40, https://doi.org/10.1016/j.epsl.2011.09.010, 2012.

Theodor, M.: Stable isotope composition of benthic foraminifera: Species-specific differences and their application, Ph.D. thesis, University Hamburg, https://ediss.sub.uni-hamburg.de/handle/ediss/6955, 2016.

Thunell, R. C. and Williams, D. F.: Glacial Holocene salinity changes in the Mediterranean Sea: hydrographic and depositional effects, Nature, 338, 493–496, https://doi.org/10.1038/338493a0, 1989.

Tsimplis, M. and Bryden, H.: Estimation of the transports through the Strait of Gibraltar, Deep Sea Research Part I: Oceanographic Research Papers, 47, 2219–2242, https://doi.org/10.1016/s0967-0637(00)00024-8, 2000.

Uitz, J., Stramski, D., Gentili, B., D'Ortenzio, F., and Claustre, H.: Estimates of phytoplankton class-specific and total primary production in the Mediterranean Sea from satellite ocean color observations, Global Biogeochemical Cycles, 26, https://doi.org/10.1029/2011gb004055, 2012.

Venkatarathnam, K. and Ryan, W. B.: Dispersal patterns of clay minerals in the sediments of the eastern Mediterranean Sea, Marine Geology, 11, 261–282, https://doi.org/10.1016/0025-3227(71)90028-4, 1971.

Weber, T., Cram, J. A., Leung, S. W., DeVries, T., and Deutsch, C.: Deep ocean nutrients imply large latitudinal variation in particle transfer efficiency, Proceedings of the National Academy of Sciences, 113, 8606–8611, https://doi.org/10.1073/pnas.1604414113, 2016.